ENHANCED MECHANICAL STABILITY OF INTERLAYER DIELECTRICS WITH SELF-ORGANIZED MOLECULAR PORES

By

AKANKSHA PANDEY

Presented to the Faculty of the Graduate School of

The University of Texas at Arlington in Partial Fulfillment

of the Requirements for the Degree of

MASTER OF SCIENCE IN MATERIALS SCIENCE & ENGINEERING

THE UNIVERSITY OF TEXAS AT ARLINGTON

August 2015

Acknowledgements

First of all, I would like to thank my advisor Prof. Choong-Un Kim for providing his continuous support and invaluable advice every step of the way throughout my research. This thesis would not have been possible without his continuous encouragement and persistent help. I would also like to thank my committee members Prof. Liu, and Prof. Koh for their valuable feedback. Also, I believe that this thesis would not have been possible without the knowledge I have gained during my two years at the University for which I would like to thank all the faculty members of the MSE department.

I would also like to thank all my current group members who helped me during the course of my research and guided me in the right direction whenever I was lost. I would specially like to thank Dr. Yoonki Sa, my mentor in Prof. Kim's group, for teaching me how to conduct effective research.

Lastly I would like to thank my parents, my brother Abhinav and my dearest friend Aaqib for encouraging and supporting me throughout my study. I dedicate this thesis to them.

June 10, 2015

Abstract

ENHANCED MECHANICAL STABILITY OF INTERLAYER DIELECTRICS WITH SELF-ORGANIZED MOLECULAR PORES

Akanksha Pandey, M.S.

The University of Texas at Arlington, 2015

Supervising Professor: Choong-Un Kim

In order to reduce resistance-capacitance delays in interconnect structures, ultralow-k films are used as interlayer dielectric materials. In most cases the preferred method to achieve the lower dielectric constant is the use of porous carbon doped silicon oxide (p-SiCOH) dielectrics. A downside of porosity in a dielectric layer during device fabrication is that it reduces the mechanical reliability of the dielectric and increases the susceptibility to adsorption of damaging materials. To overcome this and produce a material which can sustain the rigorous processes of fabrication, it is necessary to optimize the mechanical, thermal and chemical properties along with the electrical properties of the dielectric.

Processes like CMP that involve high stresses during device fabrication can cause dielectric cracking and delamination. In order to survive these processes dielectric should have sufficient mechanical strength. Apart from this, exposure to high temperature and oxidative plasma during device fabrication can damage and cause failure of the dielectric

layer. As per research conducted in our group previously, oxidative plasma environment can make the film hydrophilic and consequently assist in moisture uptake within the film. This increases the dielectric constant of the film substantially and, in essence, nullifies the effort that was put to reduce the dielectric constant in the first place. Also, treatments like annealing or plasma etching can break the long range crosslinking in the material, making it more susceptible towards viscoplastic deformation.

In order to achieve the required optimization between the electrical, mechanical, thermal and chemical properties it is necessary to focus on various ways of reducing the dielectric constant and not just the end result of achieving the lower dielectric constant. During the course of this thesis, it has been explained how subtle changes in the fabrication method can cause dramatic changes in the properties of the final product.

It has been shown in this thesis that the pores introduced through structural arrangement of atoms can provide much better mechanical and chemical reliability during the fabrication process as compared to the pores introduced through removal of large segments of material from the sample. Electrical properties of the material are measured using ellipsometer and changes in properties with processes like annealing and plasma exposure are discussed in detail. Mechanical properties of the material are measured using nano-indentation and ball indentation tests. To study the molecular structure and changes in molecular structure with processes like annealing, FTIR and XPS techniques are used. An alternative curing method for traditional subtractive films has also been proposed to enhance the material's resistance to viscoplastic deformation.

Table of Contents

List of Figures

List of Tables

Chapter 1.

Introduction and Background

1.1 Research Background of Interlayer Dielectrics

Increasing speeds of a microelectronic Integrated Circuits can, in general, be achieved by packing more transistors onto the chip i.e. by increasing the transistor density. In the past few years, this idea has been used for performance enhancement in Integrated Circuits. The reduction in the size of the transistors leads to an increase in transistor speed.[1] However, there is a limit up-to which transistor sizes can be reduced to obtain speed enhancement. After crossing a threshold this trend is reversed and the size of these complex chips, which have transistors of smaller size, starts affecting the speed negatively. This is caused by signal delays due to interconnection wiring and with each generation of scaling down, it is becoming more of a factor in increasing the overall performance of integrated systems. Overcoming this obstacle requires an understanding the cause of this trend reversal which is interconnection delay.

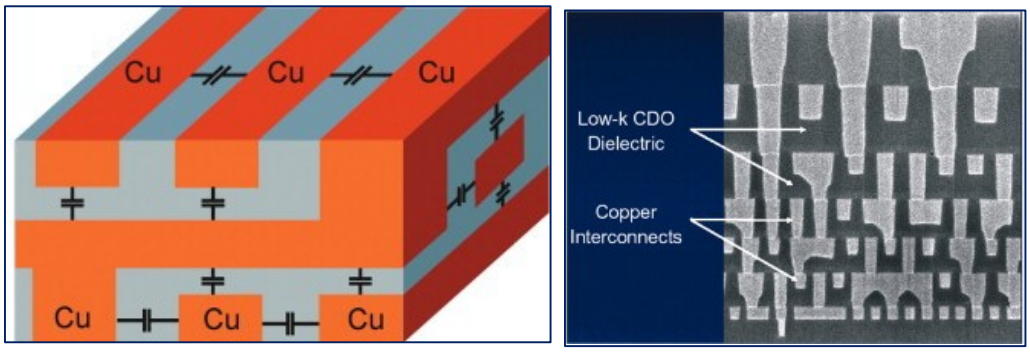

Figure 1. Schematic of copper/dielectric interlayer structure [2]

As illustrated in Figure 1, a combination of resistors, or as in this case connecting wires, and capacitors, as in this case insulating dielectric between the connecting wires,

constitutes the interconnect structure. This interconnect structure can be characterized by resistance-capacitance (RC), a unit of time. Any signal that is transmitted through this interconnect structure must experience a delay proportional to the resistance and capacitance of the structure. As we know, the resistance of a wire depends upon its cross-section area. Thus, reducing the cross-section area of the wires in interconnect, by reducing the size of the transistor, would increase the resistance. Also, since capacitance depends on the distance between two conducting plate, which in this case is the thickness of the dielectric, reduction in transistor size would increases capacitance as well. Consequently, RC delay has become the limiting factor for the modern device speed. According to Saraswat et al., the RC delay associated with the interconnect is given by the following formula

$$RC = \frac{5.53\varepsilon_0 \times \mathrm{k} \times \rho \times \mathrm{A}}{F^2{}_{min}}$$

Where,

ε_0 = permittivity of vacuum

k = dielectric constant of the insulator

ρ = resistivity of metal wire

A = area of the chip

F_{min} = minimum feature size in the chip [3]

Response speed is one of the key metrics in evaluating the quality of an Integrated Circuit. This performance metric is affected by two factors:

1. Transistor Gate Delay: which is the switching speed of the transistor
2. RC Delay / Interconnect Delay: Signal propagation time between transistors

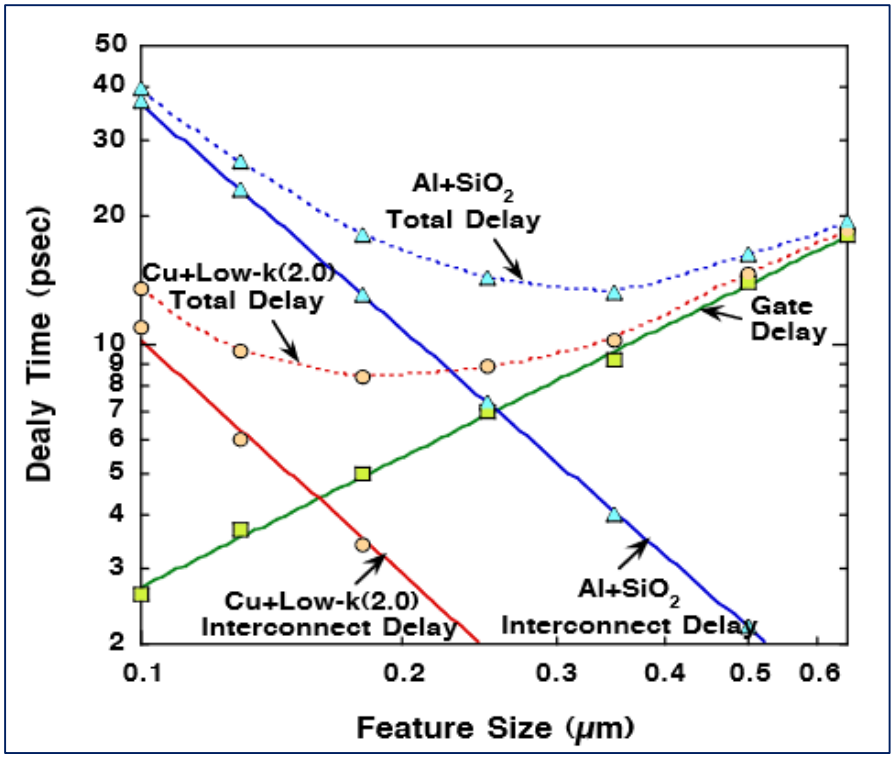

Figure 2. Device delay time vs, feature size [4]

Figure 2 illustrates how technology generation has caused a shift in the device speed limiting factor from gate delay to interconnect delay.[4], [5] Figure 2 also illustrates a comparison of two interconnect systems, namely, Aluminum with Silicon Dioxide and Copper with Low-K materials. This comparison is made because in the older devices aluminum was used for metal wiring and Silicon Dioxide (K= 4.0) was used as an interlayer dielectric. In order to reduce the RC delay as the device size decreased, Aluminum has been replaced by copper which has 36% less resistivity as compared to aluminum. Also, copper is an excellent choice because it offers great conductivity which is almost comparable to that of silver, the best conductor, at a reasonable cost. Table 1 shows the resistivity values of some of the best conducting materials available.

Table 1. Bulk resistivity of some of the best conducting materials [4]

Metal	Bulk Resistivity [μΩ-cm]
Ag	1.63
Cu	1.67
Au	2.35
Al	2.67
W	5.65

It requires a lot of research, development, and integration engineering to incorporate even the smallest material changes in the device fabrication process. In order to reduce the interconnect delay further, changing the interlayer dielectric (SiO_2, K=4.0) with a low-K material is unavoidable. However, this replacement would require a great deal of undertaking in material design and engineering. In principal, we would need to replace the interlayer dielectric with any material that has a dielectric constant lower than the traditional interlayer dielectric, i.e. lower than that of SiO_2. However, other properties like mechanical stability or chemical compatibility are also important while selecting a new interlayer dielectric material that can be integrated in the device successfully.

Dielectric constant of a material can be altered by any one or both of the following two methods and these two methods alone.

1. Decreasing the strength of the dipoles in the material
2. Decreasing the number of dipoles in the material

In order to reduce the strength of dipoles, a material with less polar bonds than Si-O bonds would be required whereas number of dipoles can be decreased simply by

reducing the density of the material. Some low-K materials with less polar bonds than Si-O like Si-F and Si-C are already being used in the industrial applications.

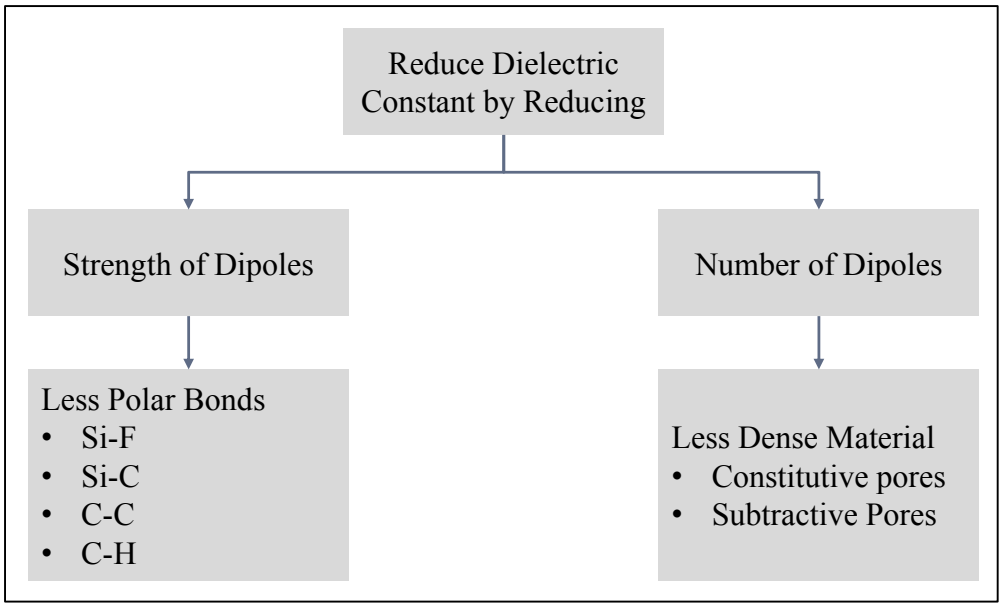

Figure 3. Methods of reducing the k value of dielectrics [2]

Figure 3 illustrates the ways in which the dielectric constant can be reduced. The most straightforward way of decreasing the dielectric is by reducing the density of a material. Density can be reduced by introducing free volume or air gaps or pores in it. Porosity can be of two types. [2], [5]

1. Constitutive
2. Subtractive

The characteristic properties of these porosities will be discussed in detail in chapter 3.

1.2 Integration Challenges Associated with Porous Low Dielectric Films

Porosity can help bring down the dielectric constant of a material. However, it also compromises the mechanical strength and chemical stability of the material, making the integration of porous materials in the device very difficult.

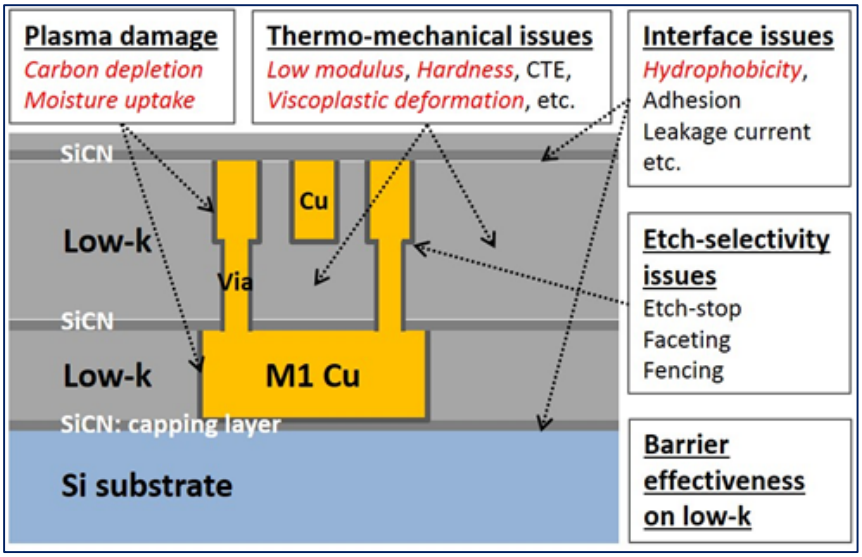

Figure 4. Integration challenges associated with porous low-k dielectrics

Figure 4 illustrates different kinds of problems faced during integration of these porous dielectric materials. Presence of pores facilitates the diffusion process hence in the absence of a barrier layer, copper may diffuse into the dielectric causing device failure.[6] SiC, SiO_2, SiCN, or SiOCNH are some of the commonly used materials for barrier layer. [7], [8], [9] Barrier layer material affects the properties of overall dielectric stack and thus the effect of barrier layer must be considered while choosing a dielectric material and a corresponding barrier layer material. Usually, the barrier layer is made up of hard, and non-porous material which means that it usually has higher dielectric constant than the porous dielectric material. Hence, integration of barrier layer, in most cases, increases the effective dielectric constant of the material. [6]

In order to be integrated successfully into the device the material should be able to withstand various mechanically vigorous processes like CMP without experiencing any failure like tearing, cracking or delamination. [8] This means that for successful integration

of these materials strong adhesion between the dielectric material and barrier layer and strong cohesion within the dielectric material is vital.

Exposure to plasma processes such as fluorocarbon plasma with oxygen which is often used for plasma etching of low-K films, also affects the electrical and mechanical properties of the low-K films. Oxidative plasma often results in chemical rearrangements and modifications in the structure of dielectric material. [10] Some of the major issues related to porous low-K film integration into the device are discussed in detail in the following sections.

1.2.1 Mechanical Instability

Increasing porosity is one of the simplest ways to produce a material with a low dielectric constant. This is an important factor in the future of interconnect technologies. However, increased porosity compromises the mechanical properties of a material like elastic modulus and hardness. [11] During the fabrication of Integrated Circuits cracking may occur under thermo-mechanical loads if the material is not mechanically strong enough. Furthermore, porosity at surface facilitates moisture uptake into the material. This harms the material in two ways; firstly it may trigger moisture assisted stress corrosion cracking and secondly since water has a dielectric constant of 80, it increases the effective dielectric constant of the overall material.

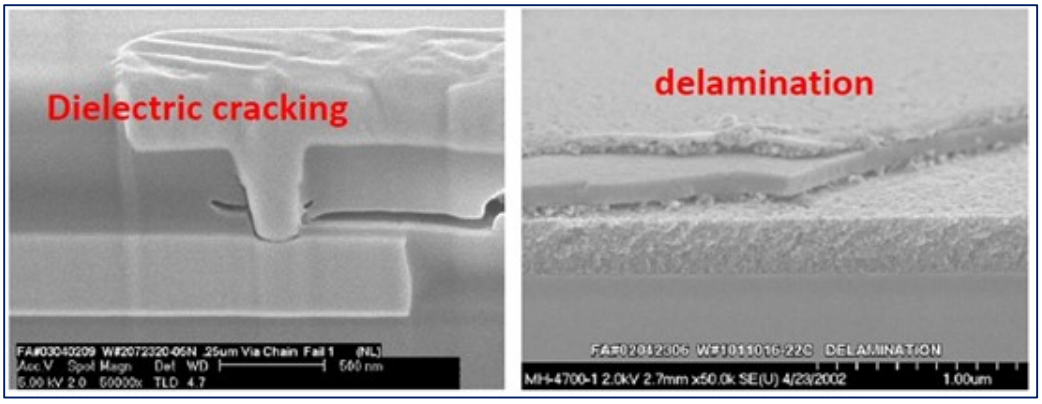

Figure 5. Examples of poor mechanical strength issues during integration

Figure 5 illustrates how vigorous mechanical processes in device fabrication cause dielectric cracking and delamination of the film from the substrate. A thorough understanding of relationship between mechanical stability, porosity and pore structure is essential to finding a suitable low-K material that can be successfully integrated into the device without failure.

The higher the elastic modulus of a material, better is the reliability of the material during the integration process. [12] However, elastic module is not the only factor which makes the material compatible for integration. Fracture toughness of the material also plays an important role in determining its compatibility for integration. Materials with low fracture toughness allow easier crack propagation hence failure may occur on application of lesser amounts of stresses. In a porous material, fracture toughness also depends on the extent of porosity and pore morphology.

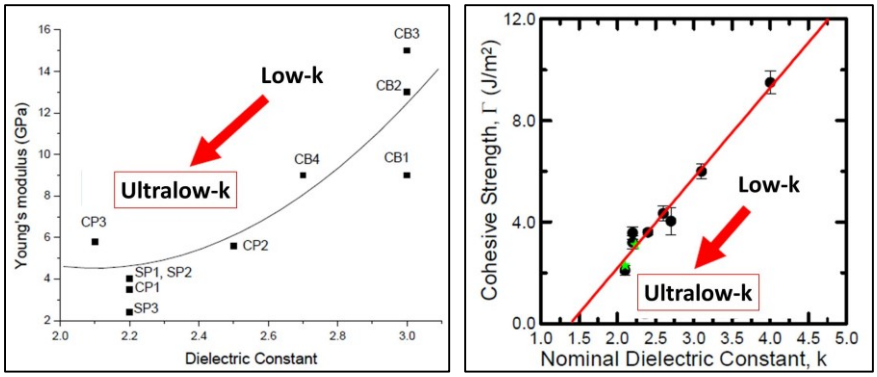

Figure 6. Mechanical property variation with porosity [13], [14]

The graphs in figure 6 illustrate that young's modulus and cohesive strength of a material decreases with decrease in its dielectric constant or with increase in its porosity. In order to explain the crack propagation process, a parameter called crack driving force is defined. In a material there are two competing forces, crack driving force and fracture toughness. Fracture resistance is the surface energy required to open up new fracture surfaces at the crack tip. Fracture resistance depends largely on the density of the film, the chemical bonding in the film, and the environment to which the film is exposed. While fracture toughness resists crack propagation, crack driving force assists it. Therefore, when crack driving force exceeds the fracture toughness of the material, fracture occurs. Crack driving force (G) can be calculated using the following formula. [15]

$$G = Z\sigma^2 h/E$$

Where,

Z = 1.096 (Dimensionless number) [15], [16]

σ = Applied stress

h = Film thickness

E = Elasticity modulus

Evidently crack driving force is inversely proportional to the modulus of elasticity and as the modulus decreases the crack driving force increases, thus the tendency of crack propagation within the material increases.

Delamination is also a serious concern during the integration process of dielectric material. Delamination can be caused by poor adhesion between the film and the substrate, which can be improved by interface engineering.[17] Treatments like plasma can improve the mechanical properties including adhesion substantially through surface densification. However, due to surface densification, such plasma treatments would compromise the electrical properties of the dielectric material by reducing the extent of porosity.[18]

CMP is not the only process where these materials experience high amount of stress. The dielectric material would also experience high amount of packaging stress affecting the lifetime of the device.[17] As the device size decreases, number of layers required in the chip increase. These additional layers also affect the reliability of the whole structure. To gain a better understanding of this affect, extensive mathematical models are employed.[17]–[21]

1.2.1.1 Viscoplastic Deformation In Porous Low-K Films And Its Root Causes

Previous experiments in our group have shown that plasma exposure causes structural changes in the PLK matrix that are responsible for creep deformation in the film. [22], [23] when dielectric material is exposed to plasma, long range cross linking is damaged and smaller clusters are formed. These smaller clusters are responsible for viscoplastic deformation in the material. When stress is applied for a longer period of time these clusters slide along cluster boundaries producing a viscous flow.

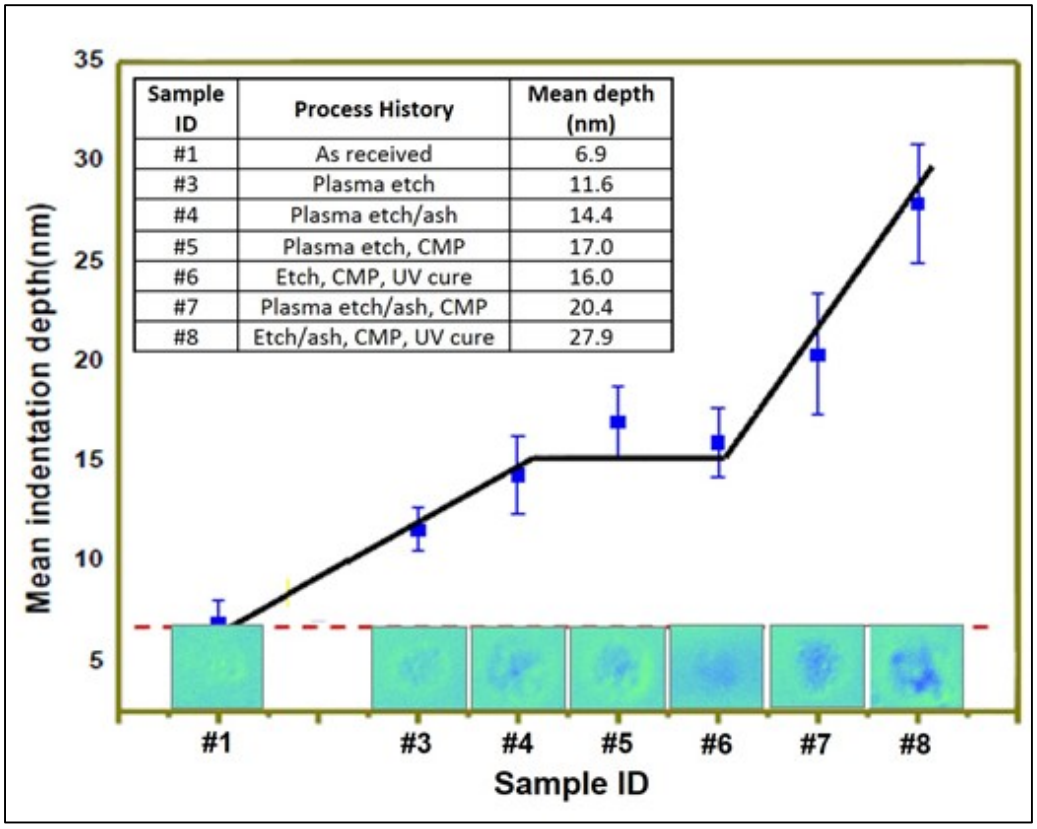

Figure 7. Viscoplastic deformation caused by various integration process [22]

Figure 7 illustrates the results of an experimental setup, where a material with a dielectric constant of 2.3, coated with 10 nm thick SiCN barrier layer is exposed to various processes employed in modern device fabrication. As illustrated, each successive device fabrication process induces additional viscoplastic deformation which accumulates over each process. Also, the level of deformation accumulated over all the processes is evident from the increase in indentation depth from 6.9 nm to 27.9 nm.

UV cure is widely used in the industry to restore the original structure of the dielectric film after the damage it suffers from various processes by removing unsaturated bonds. However, in this case as evident from the figure 10, UV cure is of little help. This is because UV cure, in most cases, is used at very high temperatures (~400^0C). Although

UV cure restores the mechanical properties of the material to some extent, it still makes the material prone to failure during integration due to the dimensional change brought by high temperature anneal. Zenasni et al. reported ~ 17% reduction in the thickness of porous low-K films after 15 min UV cure.[24] Besides, since UV cure is done using a broadband UV lamp, penetration depth is not sufficient to excite entire PLK film matrix. Apart from this, UV cure may also trigger some unintended chemical reactions like introduction of a terminal hydroxyl group which would nullify the benefits that were initially sought for by employing UV cure.

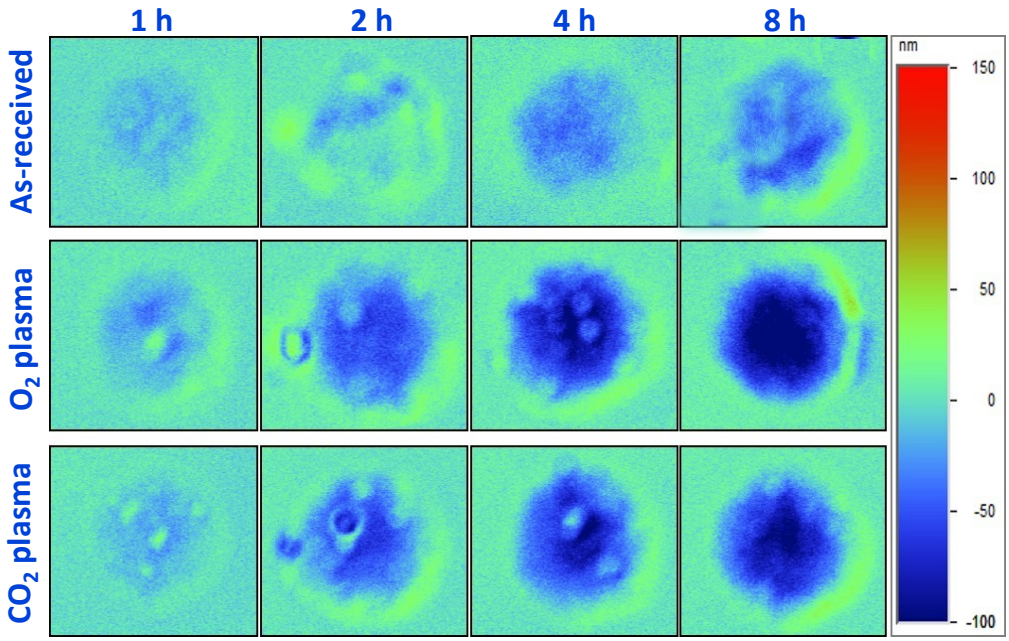

Figure 8. Residual indentation depth with different plasma exposures [23]

Figure 8 illustrates the effect of various plasma exposures on the dielectric film. Oxygen plasma is the most damaging because of its highly oxidizing nature. As discussed previously, presence of oxidizing entities in the plasma facilitate the cross link breakage and terminal hydroxyl bond formation.

1.2.2 Thermal Instability

Inadequate heat dissipation from interconnect is detrimental to the device performance. Rising temperature in the interconnect results in increasing wire resistance which causes Joule heating further raising the temperature. Higher temperature also accelerates the electromigration. In order to regulate the temperature heat must be dissipated through the interlayer matrix to a heat sink or in this case the substrate. Interlayer matrix consists of metal wires and dielectric material. Metal wires are usually good thermal conductors. In older devices non-porous SiO_2 was used as the dielectric material which was a better thermal conductor as compared to the porous low-K materials because air (pores) do not conduct heat. To understand this behavior, it is imperative to simulate the behavior of interconnects using the dielectric materials and metal wires. Delan et al., [25] who employed the transient hot wire method for their studies, reported from their studies a range of 0.11-0.19 W/mK for the thermal conductivity of the low-K materials.

Further studies have been carried out to utilize the low thermal resistance property of metals as heat carriers. One such research by Chiang et al. has suggested the use of dummy metals in interconnects for heat transportation to sinks.[26] According to their research, these dummy metals (thermal vias) can be stacked every 30 μm in a copper-polymer interconnect and 20 μm in copper-air interconnect to resemble the performance of traditional copper-SiO_2 interconnects.[26]

1.2.3 Chemical Instability

As pores are introduced in a material, its tendency to absorb fluids from environment increases. Pores also provide an easy diffusion path for other chemicals. Although porous low-K materials are usually hydrophobic due to presence of carbon,

however, once carbon gets depleted during plasma exposure the surface becomes hydrophilic. Once the surface becomes hydrophilic moisture can easily be absorbed by the surface. [27]–[34]

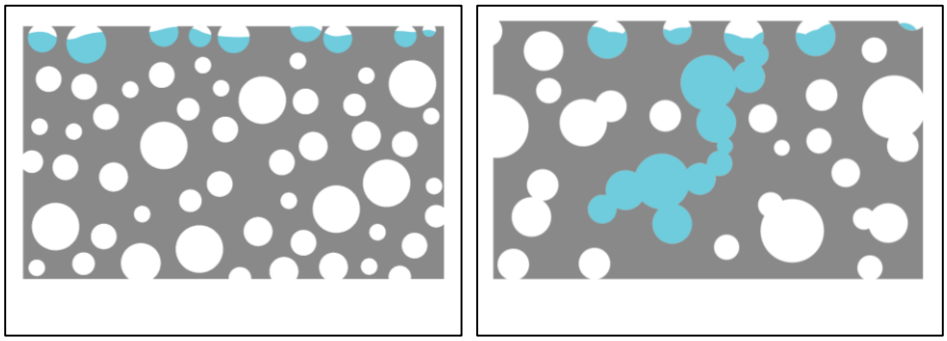

Figure 9. Fluid penetration in (a) closed pores vs. (b) open pore structure

As illustrated in figure 9, fluid absorption also depends on the pore morphology. In an open pore structure where pores are interconnected fluid can reach far greater depth than in a closed pore structure. The extent of damage increases as the thickness of dielectric layer decreases. In case of moisture absorption leakage current of the dielectric increases substantially. Also, water reduces the adhesion between the dielectric and barrier layer which may result in delamination. [35], [36]

1.2.3.1 Plasma-induced damage

Plasma etch is a process which causes extensive damage to the porous low-K film as it causes modification and rearrangement of chemical structure of the dielectric material. Low-K dielectrics usually contain carbon which make them hydrophobic in nature.

Upon plasma exposure, carbon from the surface gets depleted and the surface becomes hydrophilic. [37]–[41] This depletion is caused due to oxidation of the methyl and hydride groups in silsesquioxane to hydroxyl group. Hydroxyl group is highly

hydrophilic in nature due to its affinity towards forming hydrogen bonds with the water molecule.

As the device size decreases below 45nm, lower dielectric values are required to minimize interconnect delay. This translates into higher amount of pores and alkyl groups in the material. Hence the extent of plasma damage also increases as the technology node shrinks.

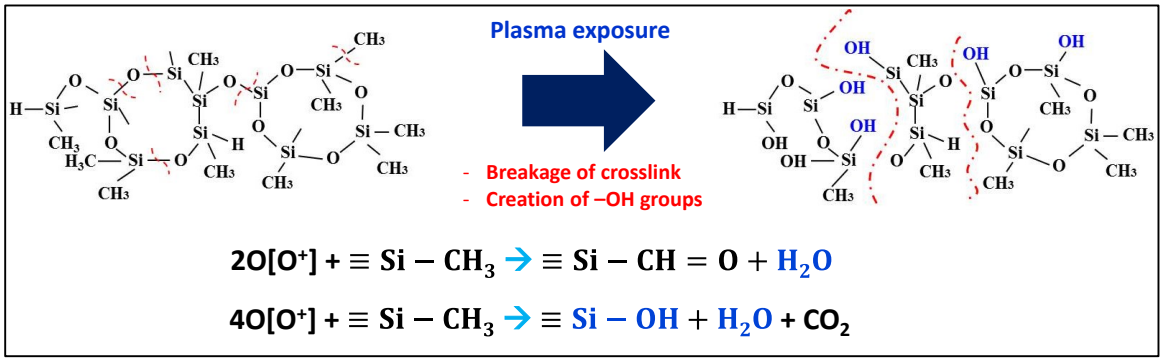

Figure 10. Description of Bond Configuration Changes by Oxidizing Plasma [22]

Figure 10 illustrates how bond configuration changes when the low-K film is exposed to the plasma. Basically plasma damage occurs in two steps

1. Breakage of desired Bonds
2. Formation new unstable bonds

In first step terminal carbon bonds and cross-linked bonds get broken. Terminal carbon bonds are responsible for creating constitutive pores. Hence the loss of these bonds results in increased dielectric constant primarily due to loss of free volume and loss of less polar Si-C bonds. Cross linking is important to provide mechanical strength to the structure. Thus when cross-linked bonds get broken, structure becomes mechanically unstable. Once the cross linked bonds are broken, the structure is left with smaller sized cluster which can slide onto each other under stress application. [22]

In second step oxygen entities present in plasma react with the broken structure and form hydroxyl and hydride bonds. Both of these bonds are formed as terminal bonds and the cross-linking that was compromised during first step does not get restored. Due to the lack of long range cross linking, the structure becomes very susceptible to visco plastic deformation.[22] Apart from that, hydroxyl bonds are highly polar bonds and result in overall increase of dielectric constant of the material. Table 2 shows the polarity of some of the bonds present in our material

Table 2. Polarity of some common bonds

Bonds	Polarity
Si-Si	0.00
Si-O	1.54
Si-C	0.65
Si-H	0.20
C-H	0.45
O-H	1.34

Chapter 2.

Experimental Setup

2.1 Preparation of Porous Low Dielectric Films

Three different types of porous low dielectric films are studied and characterized in this thesis. These dielectric films were deposited on silicon wafers without any diffusion barrier layer for easy characterization of the films. The films used in this study have a thickness of approximately 400nm and a porosity of approximately 25-35%. This porosity translates to a dielectric constant of approximately 2.0-2.4.

The CVD chamber used for synthesis of these films was cleaned using NF_3 hence residual contamination of fluorine was present in all of the samples.

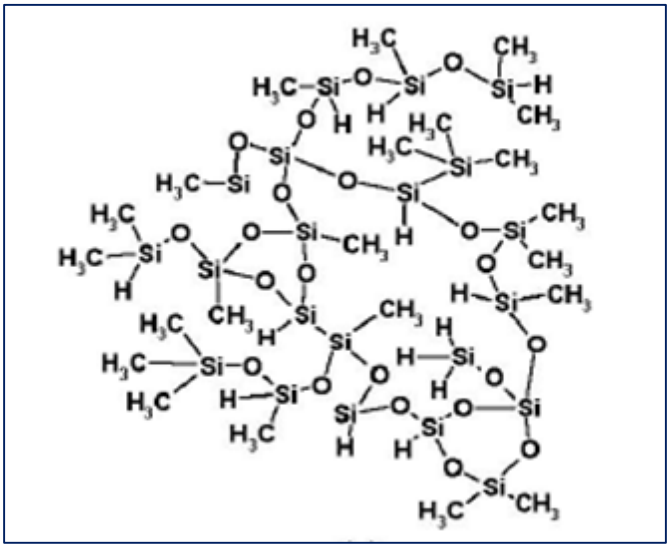

Figure 11. Networked structure of PLK film [42]

Figure 11 illustrates the network structure of porous low-K films synthesized using Plasma Enhanced Chemical Vapor Deposition (PECVD).

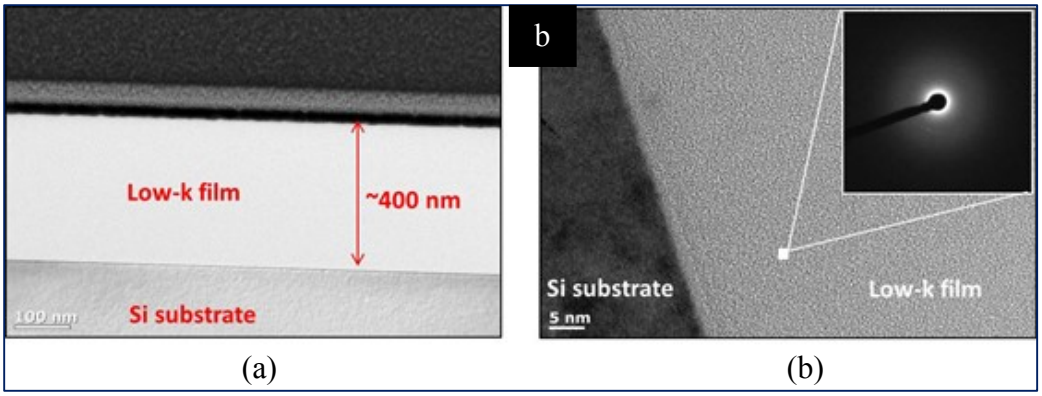

Figure 12. TEM images displaying cross-section and diffraction pattern

Image shown in figure 12 (a) is a TEM image of the sample that clearly shows that the films have very uniform thickness of approximately 400nm. Image shown in figure 12 (b) is a diffraction pattern of the sample that clearly shows that the film is porous in nature.

2.1.1 Traditional Porous Low Dielectric Film (Subtractive UV)

The porous methyl silsesquioxane (MSQ) films used in this study were synthesized using alkoxysilane matrix precursor and an organic porogen (BCHB; bicylcoheptadiene). The dual phase film was first deposited on the silicon wafer substrate using plasma enhanced chemical vapor deposition (PECVD). The dual phase film is basically SiCOH-CH_x matrix which is subsequently cured by UV radiation to remove the volatile organic fragments introduced during the initial deposition. When the organic fragments are removed, subtractive mesopores are left behind in the film. The films made using this method are referred to as Subtractive UV films throughout this study.

2.1.2 Subtractive Film with Alternative Cure Method (Subtractive AC)

The second type of films used in this study also had the subtractive porosity. These films were also deposited using plasma enhanced chemical vapor deposition (PECVD). However, the curing method for removal of volatile organic fragments (porogen) was different in this case. In case of UV cure, crosslinking of silica matrix and porogen removal occurs simultaneously. As a result, some of the porogen gets trapped inside the cross-linked matrix. This trapped porogen may escape from the matrix during further treatments that material undergoes during device fabrication. Although trapped porogen removal results in further lowering of dielectric constant, it also results in additional deterioration of mechanical properties due to introduction of extra porosity. This deterioration may result in unexpected failure of the device during fabrication. Trapped porogen may also create hindrance for crosslinking, compromising the extent of long range cross-linking.

In order to overcome the problem of trapped porogen residues, we used an alternative cure method. In this method, the sample was treated after deposition to remove the porogen without cross linking the silica matrix. Following this step the sample was cured again with UV radiation to induce cross-linking. The films made using this method are referred to as Subtractive AC films throughout this study.

2.1.3 Film with Self Organized Molecular Pores (Constitutive)

The third type of films used in this study were synthesized using porogen-less synthesis method. In this particular case, specific matrix precursor was used and the methyl group was already present in the precursor as $Si\text{-}(CH_3)_x$. The porosity in this type of films generates from terminal alkyl groups and is of the order of the size of the alkyl group

(<1nm). These pores are called micro-pores. Also this type of samples are usually rich in non-polar bonds which compensates for the less amount of porosity towards the dielectric constant. Table 3 shows the key differences between the three methods discussed here.

Table 3. Synthesis Methods for PLK Fabrication

	Subtractive UV	Subtractive AC	Constitutive
Porosity	Mesopores (Primary) Micropores (Few)	Mesopores (Primary) Micropores (Few)	Micropores (primary)
Cure	UV Cure • Simultaneous cross-linking and porogen removal	Two step cure • Porogen removal • Cross linking through UV	N/A

2.2 Characterization Techniques

2.2.1 Nano-Indentation

Nanoindentation is a frequently used technique to ascertain the mechanical integrity of films at microstructural scale. Traditional indentation characterization is limited to only bulk samples and the properties of the substrate used, may affect the results to a certain degree. Nanoindentation, on the other hand, takes on the challenges of characterizing materials at micro and nano scale.

As shown in figure 13, there are three modes in which nanoindentation can be performed: (a) depth control, (b) location control, and (c) phase control,

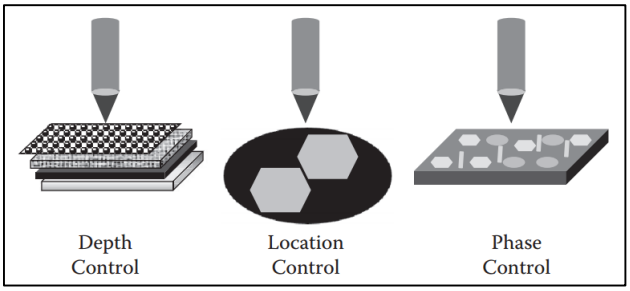

Figure 13. Different modes of nanoindentation [43]

a) Depth Control: The first mode of nanoindentation is depth control. This mode of nano-indentation is more commonly used with multilayer thin films. Li and Bhushan, in a recent work on nanoindentation, have demonstrated how the CSM technique can be used to study the hardness and modulus of the various layers of a magnetic data-storage devices.[44]

b) Location Control: This mode allows us to measure the local mechanical properties of a material at specific sites chosen for investigation. This investigation can be carried out at a microstructural scale and may or may not include microstructural defects such as grain boundaries for the investigation. [45]

c) Phase Control: Phase control mode is relevant in case of multiphase materials. In the phase control mode the mechanical properties of the sample can be studied for each of the individual phases. This however involves the identification of the different phases of the sample through the use of optical of scanning probe microscopy with a nanoindenter.[45]

For the case of our study, we use depth controlled nanoindentation technique. The first step involved measuring the elastic modulus and hardness of the specimens. Setting a penetration depth of 40 nm let us avoid any Si substrate effect in the process. Based on

experimentation, we found the conical tip to be more suitable to the thin films than other alternatives. For the sake of the experiment, we choose ten points on each of the films for analysis and carried out measurements with and approach velocity of 10 nm/s. After collecting the data, average values and standard deviation were calculated for further analysis.

2.2.1.1 Instrumentation

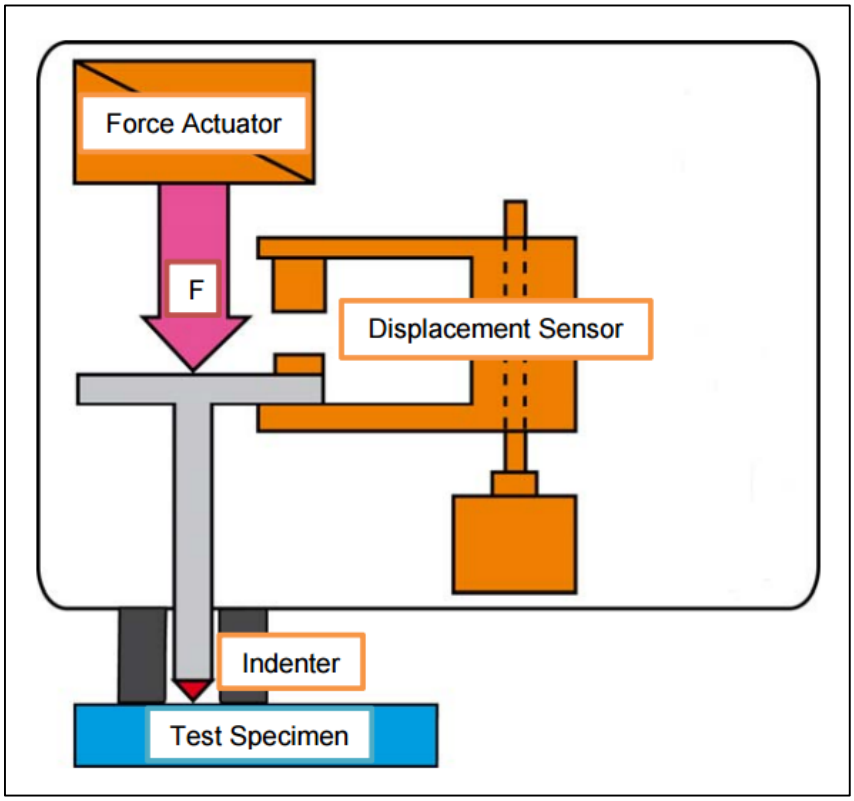

Figure 14. Schematic diagram of a nanoindenter [46]

As illustrated in Figure 14, there are three components which make up the equipment used to perform the nanoindentation experiment:

a) Indenter mounted on a rigid column

b) Actuator for applying force

c) Sensor for measuring the indenter displacements

For application of force two techniques can be used. Electromagnetically, this can be done using a coil and magnet assembly. It can also be accomplished electrostatically, in which case we can use a capacitor with fixed and moving plates or use piezoelectric actuators. Linear variable differential transducers, eddy current sensors, laser interferometers and capacitive sensors can be used to measure the displacement. A diamond is used for making indents. It is better than other alternatives like sapphire and tungsten carbide, not only because of its superior hardness and modulus, but also because its use minimizes additional measured displacement due to elastic displacement of the indenter.

For applying load on the sample, there are different indenters that can be used. One of the most durable one is the Vickers Geometry Indenter, which is used most commonly for measurements in high load nanoindentation and resembles a four sided pyramid. Another one, the Berkovich Geometry Indenter, are much more precise and sharp. They are used for precise measurements as they can cause plastic deformation with a comparatively smaller load. Unlike Vickers, they have only three sides and hence it is much easier to manufacture a precise indenter. For even better precision Cube corner indenters can be used to estimate fracture toughness at much smaller scales. Not only can spherical indenters produce elastic deformation at low loads, they can also generate entire uniaxial stress-strain curves and measure work hardening and yielding. Table 4 below lists commonly used tip geometries and their common applications.

Table 4. List of commonly used nanoindenter tips

Geometry	Application
Berkovich	Used for bulk materials and thin films greater than 100 nm thick
Vickers	Used for very large load work where the results are to be compared to other indents made with a Vickers indenter
Sharp Conical	Used for indentation and scratch testing of soft samples
Blunt Conical	used for very soft materials like polymers or biomaterials
Cube corner	Used for ultra thin films, where plastic deformation should be kept to a more confined volume
Flat punch	used for pillar or particle compression where a planar contact is desired used for extremely soft samples or in cases where a constant contact area is needed

2.2.1.2 Working Principle Of Nanoindentation

The nanoindentation process involves applying a measured force, though diamond indenter, on the sample. During loading of the indenter, the force measured as a function of the depth represents the resistance of the sample to both plastic and elastic deformation. During unloading, the decrease of force as a function of depth is defined as sample stiffness. It is a measure of sample's elastic response. Using the results from the depth sensing indentation technique, we can infer the elastic modulus and hardness of a sample.

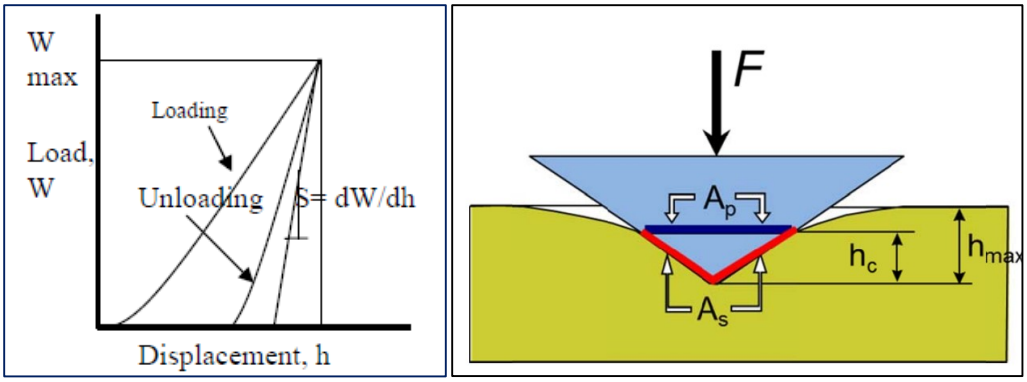

Figure 15. Load-displacement curve (left) and surface profile (right)[47]

Figure 15 above provides a schematic for understanding the nanoindentation measurement. Driving the diamond indenter into the sample causes elastic and plastic deformations. An impression of projected area Ap and contact surface area As is produced on the sample. The contact depth, hc affects the Ap and As. From this deformation, three quantities are measured for further analysis. These are

a) Maximum load W_{max}
b) Maximum displacement h_{max}
c) Elastic unloading stiffness, S=dW/dh (the slope of the initial part of unloading

The precision of the modulus of elasticity (E) and hardness (H) calculations of the nanoindentation process depend upon how accurately the three parameters defined above can be measured. At maximum load 'W_{max}' the maximum depth of the displacement is 'h_{max}' and 'h_c' represents the depth of contact of the indenter with the material under the load. On the application of the load, elastic and plastic deformations occur. On unloading, the elastic portion of the deformation is removed and the final depth of deformation is 'h_f'. The unloading curve can be approximated using the measurements above as the following power law equation

$$P = B(h - h_f)^m$$

'B' and 'm' are fitting constants for the equation. As mentioned earlier, Oliver and Pharr's method can be employed for calculations of modulus of elasticity and hardness.[47] The hardness here is defined as the ratio of the peak load applied to the projected area of contact

$$H = \frac{W_{max}}{Ap}$$

The initial part of the unloading curve can be used to define the elastic modulus as S=dW/dh.

$$\frac{1}{E_\gamma} = \frac{(1 - \nu^2)}{E} + \frac{(1 - \nu_i^2)}{E_i}$$

To make the measurement more accurate Jenny Hay et al., [48] added a correction factor to the Sneddon's equation [49] thereby arriving at the following equation

$$\mathrm{S} = \frac{dW}{dh} = \beta \frac{2}{\sqrt{\pi}} E_\gamma \sqrt{A}$$

In the equation above 'E_r' represents the reduced elastic modulus, whereas 'β' is a constant that depends on the geometry of the indenter used. Its value range from 1.0 for spherical, 1.012 for square to 1.034 for triangular. [50]

2.2.2 Ball-Indentation

The Ball indentation technique is used to study plastic deformation variation with time. In our experiment we simulate the stress that a PLK film on Si substrate experiences

while undergoing a PLK/Cu integration process. For this we apply a static weight of approximately 150 MPa using a 20 mm diameter Alumina ball. An optical microscope facilitates the observation of the indentation surface. Measurements are made using an optical profilometer equipped with Vision software. All of this equipment is enclosed in a chamber which has controls for changing various environmental conditions including temperature.

2.2.2.1 Instrumentation

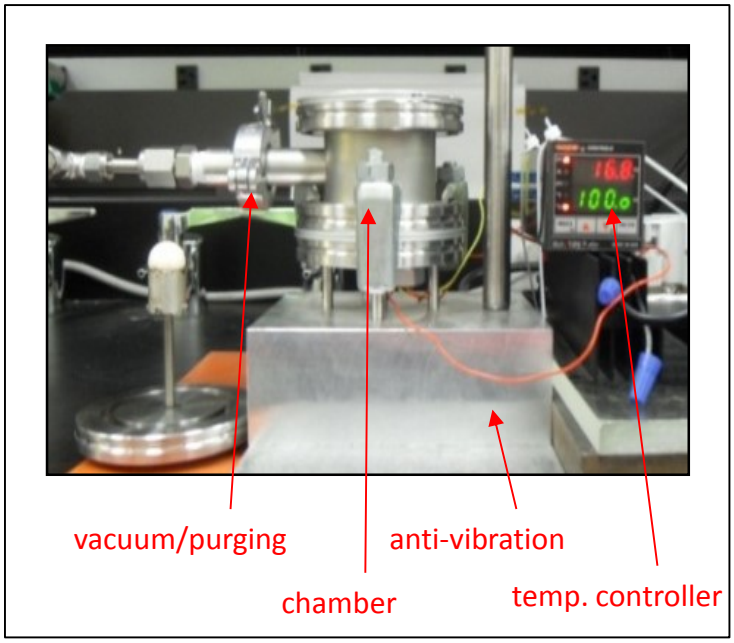

Figure 16. Ball indentation test assembly

The first step for setting up the experiment involves purifying the experimentation chamber. This is achieved by degassing the chamber by applying vacuum and Nitrogen gas purge cycle at room temperature. After the chamber is purified, an experiment temperature of 400 ˚C was set using the chamber controls. After the PLK film is loaded in the chamber Ball indentation is done by applying a static weight as mentioned previously. A setup of

the experiment instrument, including the chamber and the controls can be seen in Figure 16.

2.2.2.2 Working Principle of Ball Indentation

The time dependent deformation equation for a crystalline material for temperatures above half of the melting temperature is defined below

$$\dot{\varepsilon} = A\sigma^n$$

For the uniaxial test $\dot{\varepsilon}$ is the strain rate, σ is the applied stress, A is a material specific constant at a given temperature, n is the stress exponent of power-law creep.

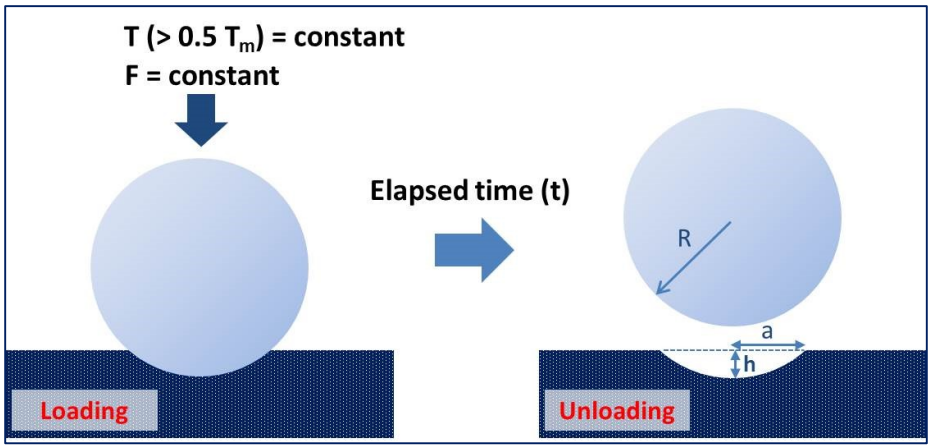

Figure 17. Indentation creep under constant load (F) with a ball indenter

Illustrated in the figure 17 are the loading and unloading processes. The Alumina ball indenter applies the static load (F) on the film at a given temperature (T). The impression created on the sample leads to a contact radius of 'a', a depth of 'h' at time't'.

In indentation creep test the pressure p_s, applied by the Alumina ball indenter, is represented by the following relation

$$p_s = \frac{F}{\pi a^2} = \frac{F}{\pi h(D-h)}$$

For the experiment where the depth of the indentation is negligible compared to the diameter of the ball (D), above equation can be approximated to

$$p_s = \frac{F}{\pi h D}$$

Using the approximation above we can also simplify the strain rate, which is defined as the ratio of indentation rate to the radius of contact at the given depth, as

$$\dot{\varepsilon} = \frac{1}{2a}\frac{dh}{dt} = \frac{1}{2\sqrt{h(D-h)}}\frac{dh}{dt} \approx \frac{1}{2\sqrt{hD}}\frac{dh}{dt}$$

From the above relation it can be concluded that the strain rate is dependent on the shape of the indenter used and the rate of indentation. Further calculations show that the depth 'h' after unloading at time't' is a measure of the plastic deformation at the given temperature and the applied load and it is related to the pressure stress. The experimental measurement of indentation depth with time on the dielectric materials provides an understanding of the viscoplastic deformation in these materials.

2.2.2.3 Optic Surface Profilometer

For measuring indentation depth after ball indentation test, a WYKO® optical profiler NT9100™ was used, which provides highly accurate surface topographic measurements. It achieves this through a combination of non-contact interferometry with advanced automation.

Figure 18 shows a schematic for the working of WYKO® NT9100™ optical profiler. An illuminator is used to shine light on the objective through an IMOA (Integrated Modular Optics Assembly). A beam splitter is used to split the incident light into two beams a reference beam and a test beam. The reference beam is reflected off of the reference mirror in the objective. The test beam, on the other hand, reflects off of the sample back to the objective. The light that the camera finally receives, is an interference pattern created by the recombination of the two beams. The Vision software, that the profiler is equipped with, processes the light signal and produces a visual of the sample surface for analysis.

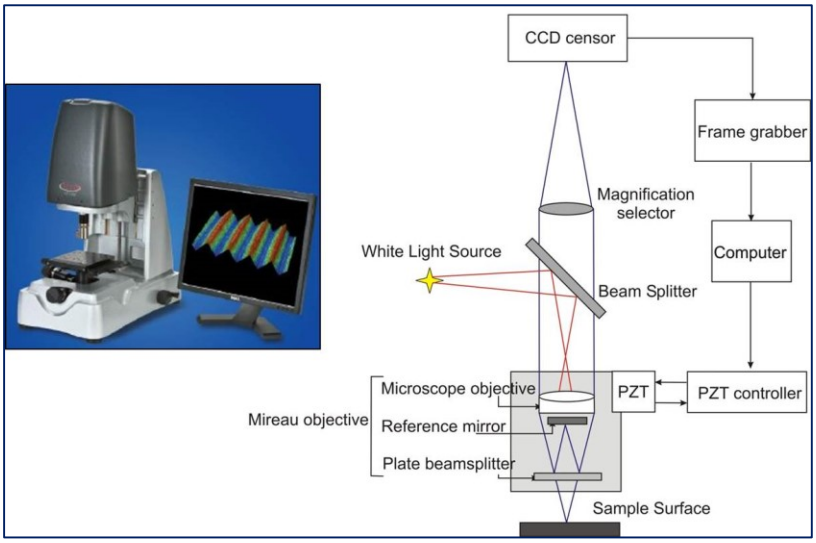

Figure 18. Schematic diagram of optic surface profilometer

For the case of our experiment, a newer technique called the Vertical Scanning-Interferometry (VSI) which uses phase-shifting interferometry, was used to study the sample surface and indentation depth. Although the working principle of VSI is similar to other interferometry where light beams reflected from reference mirror and sample

recombine to produce interference patterns, the measurements that a Vertical Scanning-Interferometry does for creating the sample surface are different. In the Vertical Scanning-Interferometry mode an unfiltered white-light source is used for the experiment and instead of measuring the phase of the interference fringes created, it measures the degree of fringe modulation. The sequence of steps from incidence of lights to recombination to form interference fringes is similar to that described in the previous section. However, for the measurement, a stepper motor is used to move the objective in a vertical direction to scan the sample surface at varying heights. This overcomes the shortcoming that a short coherence length of white light has in producing fringe patterns. A peak for the fringe contrast is achieved as a result of measurements being taken at different heights as the sample translates through focus.

For each point on the surface an interference signal is recorded as the system scans the surface of the sample. The software then uses the signals to arrive at the vertical position which corresponds to the peak of the interference signal for the given point on the sample surface.

2.2.3 Ellipsometry

Spectroscopic Ellipsometer are widely used for determination of film properties like thickness, extinction coefficient and refractive index because of the ease and speed with which they can be operated. The working principle of a spectroscopic ellipsometer is based on the light polarization that occurs due to reflection and transmission at the film interface. For the case of our experiment we used spectroscopic ellipsometer for testing the thermo-mechanical stability of the samples.

Three specimen of each sample were used for the experiment. The first specimen of each sample was the sample in its original, as received state while the second specimen of each sample was annealed at a temperature of 400^0C for 1 hour. The third specimen of each sample was exposed to plasma. Plasma source used in this study was O_2/Ar, the power used was 50 W and plasma exposure time was 20 min. Using spectroscopic ellipsometer changes in light polarization were measured for three angles in the range of 65 and 75 degrees.

2.2.3.1 Instrumentation

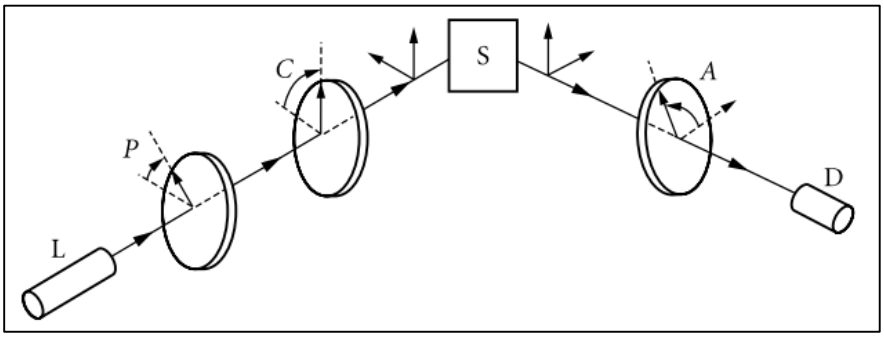

Figure 19. Schematic of spectroscopic ellipsometer [51]

Figure 19 illustrates the various working components of a spectroscopic ellipsometer. Light source (L), polarizer (P), compensator (C), sample (S), rotating analyzer (A) and a detector (D) form the constituents of a spectroscopic ellipsometer. The light source emits unpolarized light which after getting polarized by the polarizer gets reflected and transmitted at the film interface. This light, which is elliptically polarized, is passed through an analyzer and a detector to measure the change in the polarization.

2.2.3.2 Working Principle of Ellipsometer

Ellipsometer is used to measure the change in polarization of light. Ψ and Δ are quantities which define the change in amplitude and phase, respectively, which the components of electric vector experience, parallel and perpendicular to the plane of incidence of light. These quantities form the basis for the determination of properties of a given sample such as dielectric constant, thickness and refractive index. The incident light has two components of polarization state represented by s component (oscillating parallel to sample surface) and p component (oscillating parallel to plane of incidence). Furthermore, a complex reflection ratio (ρ) is defined as the ratio of Rp and Rs where Rp and Rs are the intensity of p and s components (described above) after reflection.

$$\rho = \frac{R_p}{R_S} = \tan\Psi\, e^{i\Delta}$$

The above equation [51] represents the relation between the quantities defined previously. In the equation of complex reflection ratio, $\tan\Psi$ defines the amplitude change on reflection. Ellipsometry is extremely accurate and because of the simplicity of its computation it is easily reproducible too. Amplitude and phase changes measured using the calculation above are then used in a mathematical model to get the properties of the given sample. For the case of our calculations the film being examined has pores and is not completely homogenous. Since, traditional ellipsometry calculations use discrete, isotropic and optically homogenous films, we had to tweak the approach to get results for our non-homogenous film samples.

2.2.4 Fourier Transform Infrared Spectroscopy

Fourier Transform Infrared Spectroscopy (FTIR) is a very popular technique for characterizing bonding and molecular structure of dielectric materials. The working principle of FTIR is the infrared absorption by dipole-photon interaction.[52] For the case of our experiment, Fourier Transform Infrared Spectroscopy was performed using a baseline corrected FTIR spectra. This spectra was obtained in transmission mode over 750-3500 cm^{-1} at a resolution of 2 cm^{-1} averaged over 128 scans. For the purpose of backbone structure characterization, deconvoluted fitting of siloxane (Si-O) backbone peak was used. For peak deconvolution, all peaks were assumed to perfectly follow the Gaussian function.

The first step in the collection of the FTIR spectrum is the collection of the spectrum of a bare Si substrate to differentiate it from that of the sample. After this the spectrum of the low-k dielectric on the Si substrate is collected and using the previous spectrum as the background, the spectrum of just the low-k dielectric can be obtained. Figure 20 illustrates the typical FTIR spectrum of a porous SiCOH dielectric which show various absorption bands. These broad bands are a result of the diversified fil structure from the plasma polymerization process.

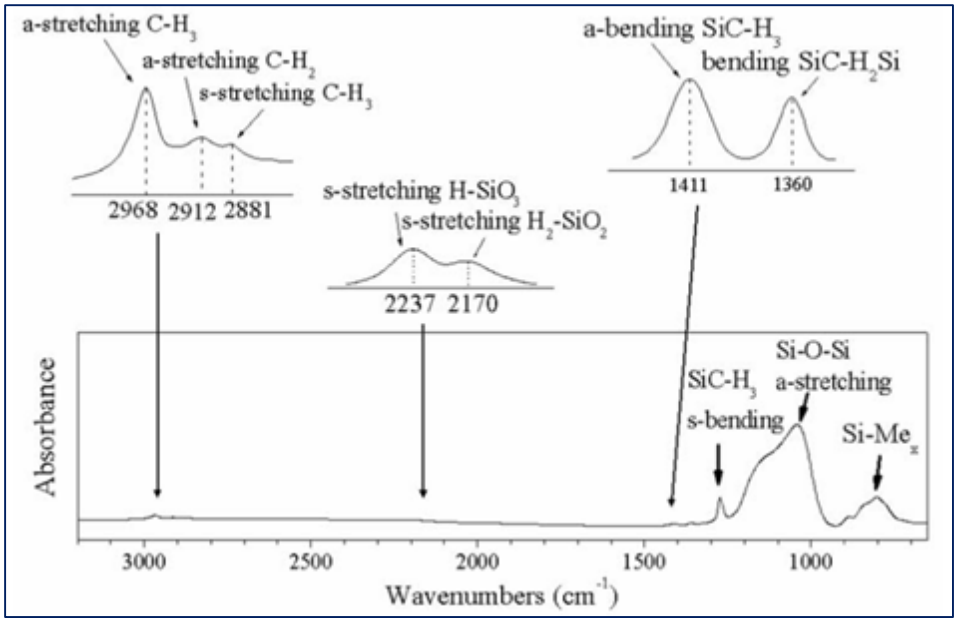

Figure 20. Representative FTIR spectrum of porous organosilicate [53]

Peak assignments for the peaks observed in the figure 20 are listed in Table 5 For example, the Si-O-Si bond, which seems like part of a siloxane network, is responsible for the band from 1200 to 950 cm^{-1}. From the peaks observed above three distinct configurations of the Si-O-Si bonds can attributed to three different peaks. These structures are the cage at 1135 cm^{-1} (Si-O-Si~150º), the network at 1063 cm^{-1} (Si-O-Si~140º), and the linear at 1023 cm^{-1} (Si-O-Si<140º). [42]

The central force model and its equation proposed by Sen. Et al. [54] can be used to assign wavenumbers to their corresponding Si-O-Si bridging angles

$$\omega^2 = \frac{\alpha}{m_0}(1 - \cos\theta) + \frac{4\alpha}{3m_{Si}}$$

In the equation, ω represents the angular frequency, α represents the Si-O bond-stretching constant, m_0 represents the atomic mass of oxygen, and θ represents the Si-O-Si bridging angle and m_{Si} represents the atomic mass of silicon. From the above equation it

can be concluded that wavenumber (which is proportional to angular frequency) increases with increase in the Si-O-Si bridging angle α. Reduction in density and formation of pores are a direct consequence of large α values which ultimately results in low dielectric constant values. [42]

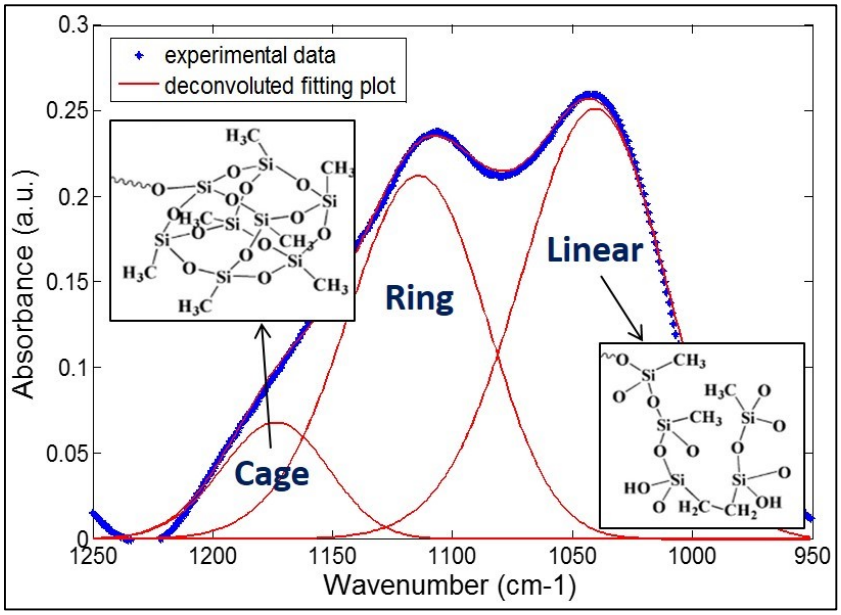

Figure 21. Deconvolution of the Si-O-Si asymmetric band [42]

Figure 21 illustrates the three types of structures that make the backbone of porous organosilicate film. The properties and characteristics of these structures will be discussed in detail in chapter 3.

Table 5. FTIR peak assignments of SiCOH low-k Dielectrics [42]

TMCTS	$k=2.8$	$k=2.05$	Mode	Comment
2968	2969	2968	ν^a C–H_3	sp^3 CH_3
2906			ν^s C–H_3	sp^3 CH_3
	2916	2932	ν^a C–H_2	sp^3 CH_2
	2880	2875	ν^s C–H_2	sp^3 CH_2
	2232		ν^s Si–H	H–SiO_3
	2178		ν^s Si–H	H–SiO_2Si
2165			ν^s Si–H	H–SiOSi
		1740, 1714	ν C=O	As deposited only
		1461	δ C–H_2	CH_2 isolated from Si
1405	1412	1412	δ^a C–H_3	$SiMe_x$
	1358	1379	δ C–H_2	Si–CH_2–Si
1259	1273	1274	δ^s C–H_3	$SiMe_x$
	1135	1140	ν^a Si–O–Si	Cage Si–O–Si angle ~150°
			ν C–O	Si–O–C
1063	1063	1065	ν^a Si–O–Si	Network (network) Si–O–Si angle ~144°
	1023	1035	ν^a Si–O–Si	Silicon suboxide, Si–O–Si angle <144° D_{3h} ring structure
	890		δ H–Si–O	H–SiO_3
			ν Si–C, ρ^s CH_3	$SiMe_2$
865			δ H–Si–O	H–SiO_2Si
	848	843	δ H–Si–O	Network smaller angle
			ν Si–C, ρ^a CH_3	$SiMe_3$
	802	800	ν Si–C, ρ^a CH_3	$SiMe_2$
754			ν Si–C, ρ Si–CH_3	$SiMe_1$
	773	779	ν Si–C, ρ CH_3	$SiMe_1$
			ν Si–C, ρ^s CH_3	$SiMe_3$
710	730	720	ν^s Si–O–Si	
	440	440	δ of O–Si–O	Network and ring opening vibrations

2.2.4.1 Instrumentation

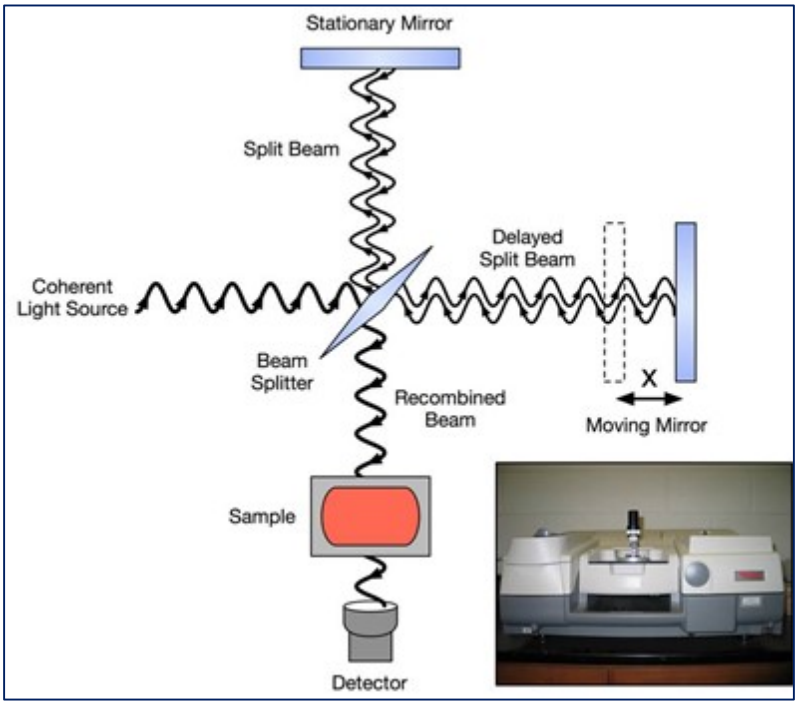

Figure 22. Schematic illustration of FTIR

Figure 22 illustrates the instrument details for an FTIR. An IR beam is made incident onto a beam splitter using a collimating mirror. Two beams, one directed towards a fixed mirror and another towards a moving mirror result upon the beam split. The two beams are combined after reflection to form a beam with a particular phase difference. This beam is then directed towards the sample. The moving mirror can be adjusted thereby affecting the phase of the recombined beam. A detector is present at the end of the sample to collect and measure the intensity of the beam transmitted through the sample. The moving mirror is used to change the optical path length and hence the intensity of the transmitted beam.

2.2.4.2 Working Principle of FTIR

FTIR's working principle is based on Michelson Interferometer principle.[55] Atomic vibrations like asymmetric and symmetric stretching, in-plane and out-of-plane bending correspond to IR range for absorption. IR absorption can occur if the energy of the IR photons correspond to the difference in energy levels of two vibration modes. Beer-Lambert's law describes how absorbance (A) depends on the molar absorptivity (α), film thickness (t), bond concentration (c) and the intensities of incident (I_0) and transmitted light (I_1)

$$A = -\log\left(\frac{I_1}{I_0}\right) = \alpha \cdot c \cdot t$$

For the purpose of our study, a Nicolet^{TM} 6700 Spectrometer was used in the transmission mode. The FTIR chamber was purged of moisture and carbon dioxide using Nitrogen gas. The beam incident on the sample for capturing the spectrum had the following properties: ~4 cm^{-1} wavenumber resolution, ~4000 cm^{-1} – 520 cm^{-1} wavenumber range (which correspond to IR), ~ 256 number of scan.

2.2.5 X-ray Photoelectron Spectroscopy

FTIR is a versatile technique, however in the case of low-k films there is an inherent shortcoming. FTIR spectroscopy, because of the penetration of the IR beams into the sample, produces results which correspond to the bonding in the bulk material and not just the film. To overcome this shortcoming, X-Ray Photoelectron Spectroscopy (XPS) is used which, unlike FTIR, is sensitive to the surface bonding configuration. For the case of our experiments, a Perkin-Elmer Phi 560 XPS/Auger System was used. The source of the X-

ray beam in the instrument was a monochromatic 1486.7 eV Kα Al with 0.16 eV energy width with the ultimate energy resolution of the spectrum being 0.4-0.6 eV.

To examine the film strength, we sputtered the surface of the film with Argon ions. Since, for each sample, same thickness dielectric films were deposited on top of Si substrate, time-dependent scanning normal to the Si substrate with continuous sputtering provided the time to reach the substrate. For a stronger matrix film, time taken to strike the surface of the substrate silicon would be longer than it is for a weaker matrix film.

2.2.5.1 Instrumentation

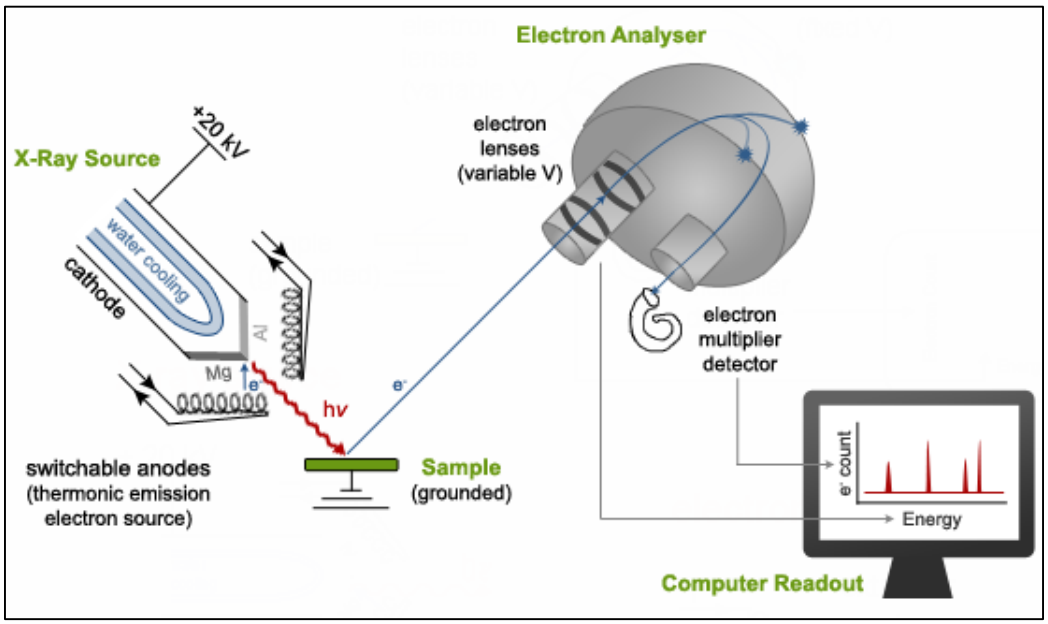

Figure 23. Schematic of X-ray photoelectron spectrometer [56]

The schematic of a XPS instrument is illustrated in Figure 23. The collection and analysis of all photoelectron is done in an Ultra High Vacuum (UHV). Apart from the X-ray source, the instrument has an electron analyzer which contains a photoelectron spectrometer to collect and analyze the photoelectrons. The spectrometer consists of

electrostatic lenses and steering voltages which allow the selection of photoelectrons of a particular kinetic energy which are then directed to the electron multiplier detector. Apart from non-conducting materials which require special treatment, all non-volatile samples can be analyzed using XPS.

2.2.5.2 Working principle of XPS

Unlike FTIR, XPS is sensitive to surface bonding configurations. Surface atoms have electrons which absorb the incident X-ray photons and get enough energy to escape the surface. These photoelectrons are then detected by a spectrometer and their kinetic energy is analyzed in the electron analyzer. Since the energy of the incident X-ray as well as the kinetic energy of the photoelectrons is known the following equation can be used to determine the binding energies of the electrons

$$E_B = h\nu - E_K - e\varphi$$

In the above equation,

E_B = binding energy of core level electron

$h\nu$ = energy of X-ray photons

E_K = kinetic energy of ejected photoelectrons and

$e\varphi$ = work function of the detector.

The binding energy, as calculated here, represents the energy that is required to release an electron from its orbit and are used to identify a material. For the case of our study binding energy values used are C_{1s} which is approximately 285 eV and Si_{2p} which is approximately 103 eV.

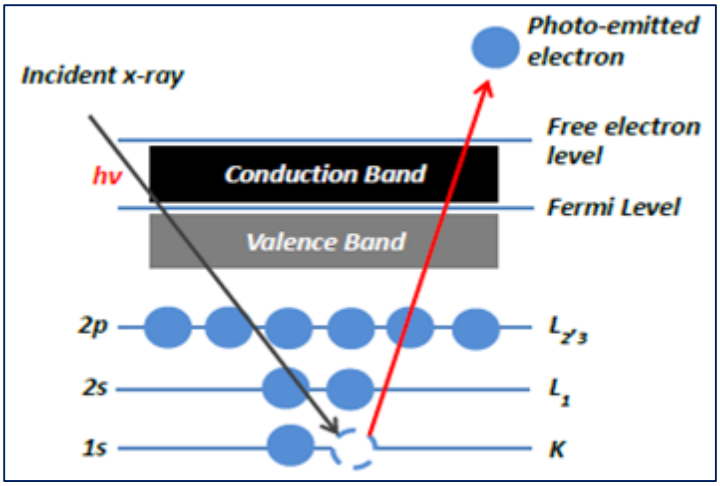

Figure 24. Principle of x-ray photoelectron spectroscopy [57]

As depicted in the figure above, the detection depth is low in XPS, usually less than 10 nm, and depends on the material being examined. This makes it sensitive to surface bonding configurations.

Chapter 3.

Characterization and Comparison of Porous Dielectric Films

3.1 Porosity

As mentioned in chapter 1, porosity can be of two types.

1. Constitutive
2. Subtractive

The first one is the one that arises from the structural arrangement of the atoms in the molecular structure of the material. This type of porosity is called constitutive porosity and the pores are referred to as constitutive pores. Such materials are porous right after synthesis without any additional treatment requirements. As constitutive pores are generated within the structure by the spatial arrangements of atoms or cluster of atoms, their size is also of the order of those cluster of atoms. Constitutive pores are usually very small in size (<1nm) and are often called micro-pores. [2], [11] In case of periodic molecules, pores tend to be distributed periodically across the structure. Also, constitutive pores are almost never interconnected and are closed pores. Constitutive porosity is usually very low (<15%). [2], [11]

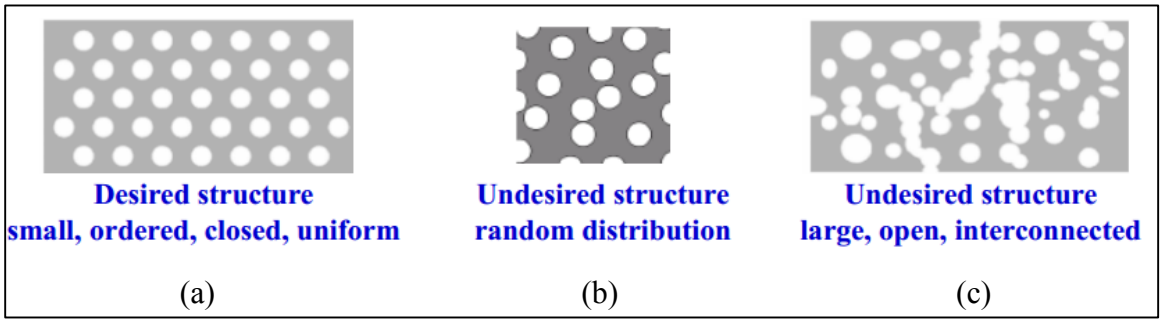

Figure 25. Types of pore structures

In case of our constitutive sample porosity arises from terminal methyl group hence the size of the micro-pores in this case is of the order of the size of methyl group. However, we expect these pores to be closed because merging of two or more pores is highly unlikely in case of constitutive pores. The structure of our constitutive sample should look like the one illustrated in figure 25 (b).

The second kind of porosity arises from the selective removal of the material from the bulk material. This type of porosity is called subtractive porosity and the pores are referred to as subtractive pores. Subtractive porosity is introduced through two step process. The first step is to form a dual phase bulk material with volatile, thermally degradable substance, commonly referred to as porogen, as the second phase along-with the desired phase. This volatile phase is removed by additional treatments like annealing after synthesis to introduce pores. Subtractive pores are usually quite large as compared to constitutive pores (>2nm and up to tens of nanometers) and are often called mesopores. [2], [11] Subtractive pores lack the structural periodicity that may be observed in the constitutive pores. Subtractive pores are often interconnected open pores as shown in figure 25 (c). Subtractive porosity can be as high as 90%. [2], [11]

In case of our subtractive samples, pores are expected to be large and interconnected as illustrated in figure 25 (c). These type of pores prove to be very harmful in environments where fluid absorption may occur. Fluid can penetrate deeper into these structures due to the pore interconnectivity thus damaging the whole film instead of the surface. In case of the constitutive films, however, the damage or fluid absorption is restricted to the surface because pores are not interconnected.

Also, structure with interconnected and larger pores is mechanically weaker than the structure with closed and smaller pores because the applied stress is more uniformly distributed across the surface of the smaller closed pore structure. As mentioned in chapter 2 we have two types of subtractive samples, Subtractive UV and Subtractive AC. Both of these samples are expected to have similar pore structure in terms of pore size, pore distribution, and pore connectivity.

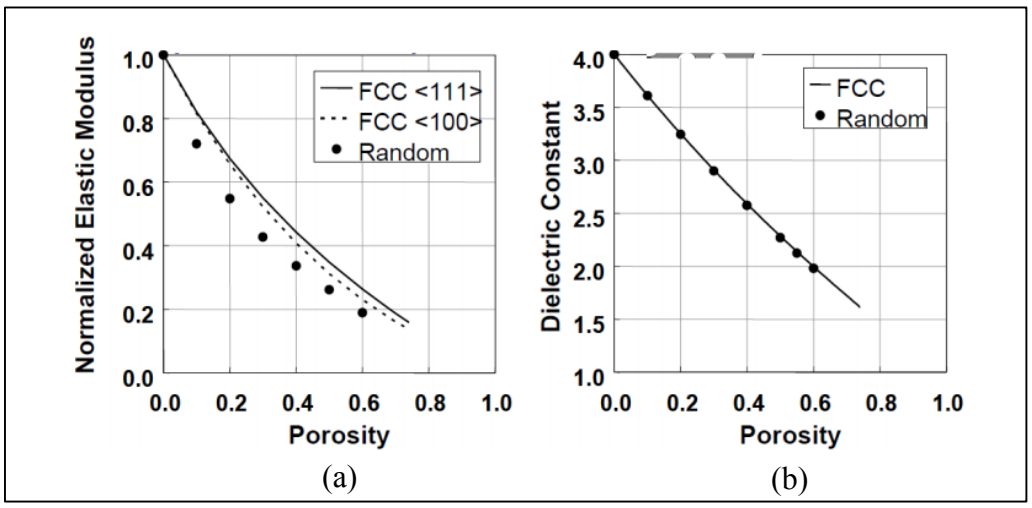

Figure 26. Elastic Modulus Variation with Pore Uniformity [58]

According to a study conducted by M. Miyoshi et al, pore distribution can affect the mechanical properties significantly.[58] The graph in figure 26 (a) shows normalized elastic modulus change as porosity increases. Normalized elastic modulus is the ratio of elastic modulus of porous film and bulk material. It is evident of the graph that when pores are distributed uniformly, higher modulus at same porosity may be achieved. The graph clearly shows that it is possible to increase normalized elastic modulus by 20-30% for the same porosity material by making the pore distribution uniform.

3.2 Thickness and Dielectric Change with Annealing & Plasma Exposure

We tested our samples for thermo-mechanical stability by measuring the change in the dielectric constant and film thickness after annealing and plasma damage in the films.

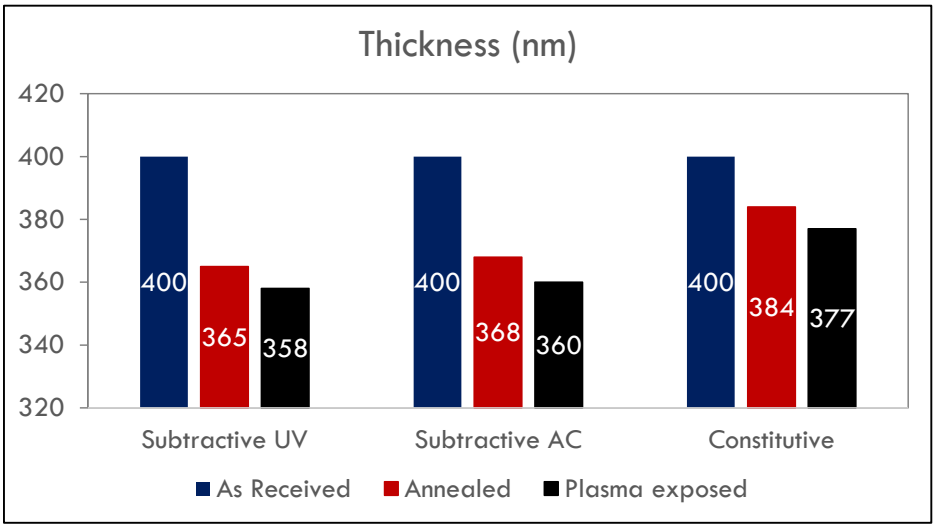

Figure 27. Change in film thickness with annealing and plasma exposure

As illustrated in figure 27, the thickness reduction of subtractive films after thermal annealing was about 10% and that of structural film was about 4%. This trend was extended to the plasma damaged samples as well which indicates that the extent of damage causes by such treatments is less intense in case of constitutive film as compared to the subtractive films.

Increased porosity of a material results in higher active surface area, which makes the porous materials more susceptible to the damage from thermal stress as well as to the damage from reactive chemical entities involved in plasma etching during back end of the line integration process. Damage susceptibility is further increased when these pores are interconnected and not sealed. In case of open, interconnected pores oxygen radicals and ions generated during plasma etching can penetrate much deeper into the sample than in

case of closed pore structures. These radicals and ions react with methyl moieties at the surface of the dielectric film and form hydroxyl terminal bonds. In this process the already unstable pores collapse resulting in film thickness reduction. Constitutive sample has smaller closed pore structure, which is why plasma damage is restricted to the exposed surface. Hence, the extent of reduction in film thickness is much smaller than both the subtractive samples. This strengthens our porosity model and assumption that constitutive samples have better thermo-mechanical stability as compared to the subtractive porosity samples.

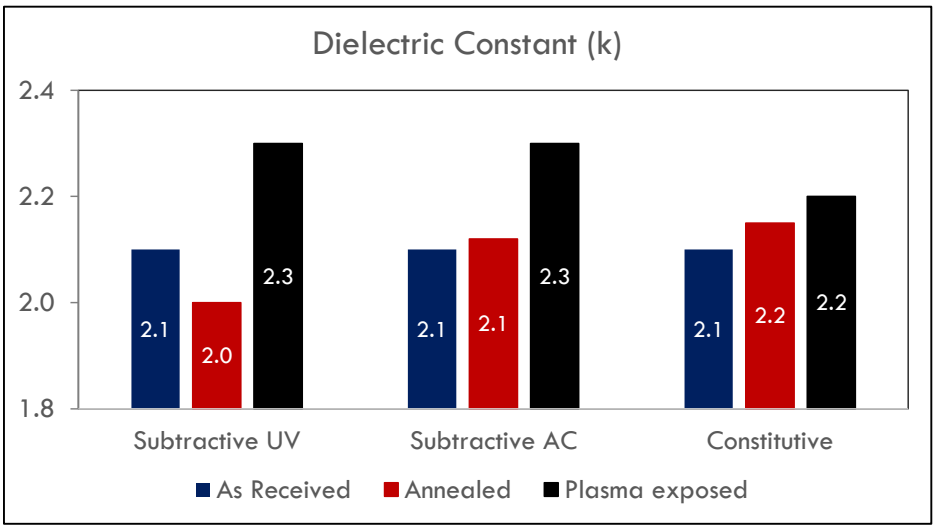

Figure 28. Change in dielectric constant with annealing and plasma

We also measured the dielectric constant of our samples along with the thickness. As illustrated in figure 28, dielectric constant of the all received films without any treatment was 2.1. Here, we observed a very interesting phenomena. Dielectric constant of the Subtractive UV film further decreased after thermal annealing. We expect this to be happening due to the removal of labile porogen residue that was trapped into the sample due to simultaneous crosslinking and porogen removal process during cure process of

subtractive UV sample. In case of subtractive AC sample, negligible amount of labile porogen residue is present, which is why this effect is not visible in that sample. Constitutive sample experiences some increase in dielectric constant due to the surface damage.

The graph in figure 28 also demonstrates that subtractive films are more prone to the damage caused by plasma exposure in terms of electrical properties. This is because when exposed to plasma, dielectric films experience loss of methyl moieties as Si-CH_3 bonds are broken. This bond breakage causes dangling bonds at the surface, which react with moisture or oxygen radicals and ions present in plasma to form terminal hydroxyl bonds (Si-OH). Hydroxyl group, due to its affinity towards water, makes the surface hydrophilic. This later results in moisture uptake from the environment and since water has very high dielectric constant, even the smallest amount of moisture uptake can increase the overall dielectric constant of the film substantially.

3.3 Mechanical Strength

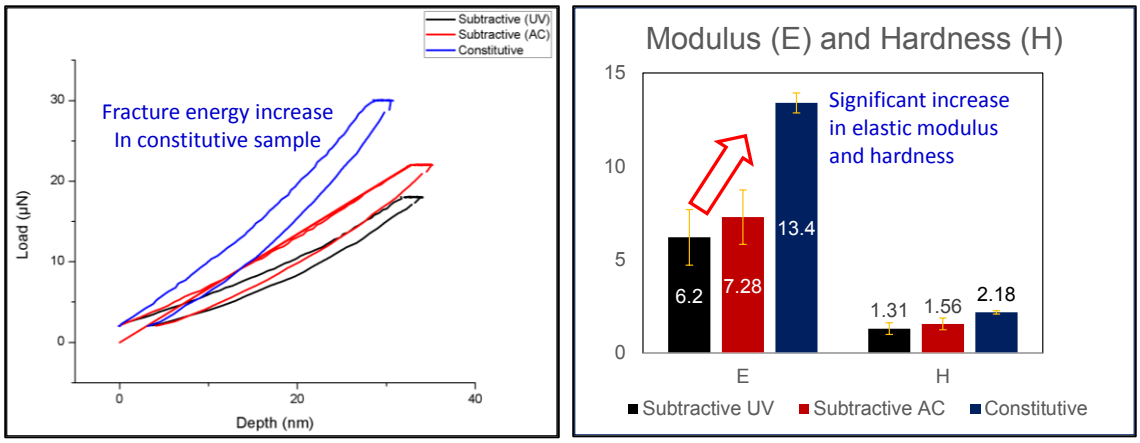

Figure 29. Comparison of elastic modulus and hardness

In order to characterize the mechanical strength of our sample we used nano indentation technique. Constitutive sample had much better mechanical properties as compared to the subtractive samples. For constitutive sample elastic modulus was measured to be 13.4GPa, which is considerably better than previously reported porous organosilicate thin films with similar dielectric constants. Subtractive films, however, were not competitive enough with elastic modulus reaching only up to 6.2 GPa for Subtractive UV and 7.3 GPa for Subtractive AC. In order to make the film usable in industry, elastic modulus of at least 10 GPa is required. Hardness of the samples also follows the same trend as elastic modulus. The measured hardness of the constitutive film was 2.2 GPa and that of subtractive UV film was 1.3 GPa. While subtractive AC showed slightly better hardness of 1.6 GPa than subtractive UV sample, it was still inferior than that of constitutive sample. The values shown in the graph are mean values.

We also calculated the Standard deviation for these values. For elastic modulus, the standard deviation in case of constitutive sample was found to be 0.5 GPa whereas the same in case of subtractive samples was found to be about 1.5 GPa which strengthens our hypothesis that the pores in subtractive sample may not be uniformly distributed.

3.4 Creep Resistance

Following the nano-indentation, we also tested our samples for visco-plastic deformation using ball indentation test. Viscoplastic deformation was not considered to be a serious issue for the interconnect system a decade ago. However, with the scaling of the interconnect system, dimensional change brought by viscoplastic deformation on prolonged exposure to stress environment, has become significant.

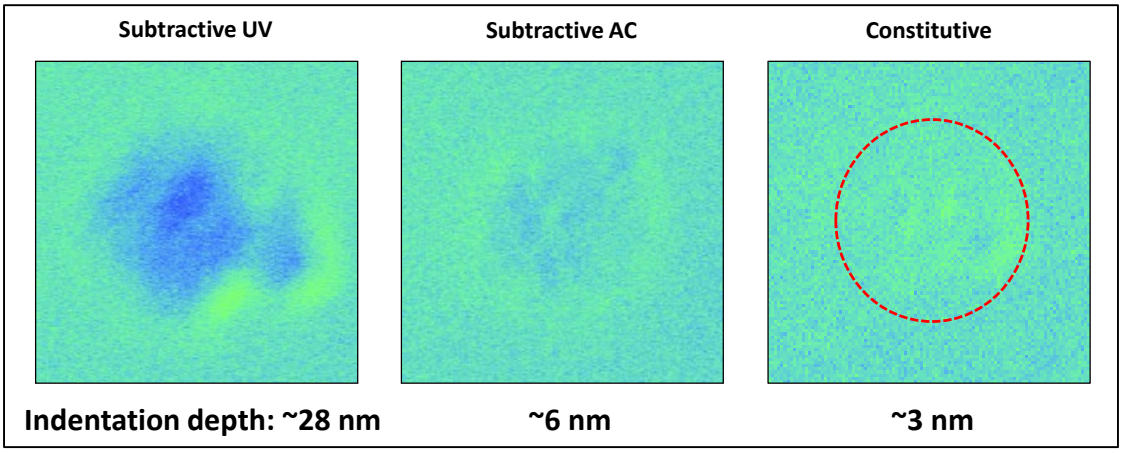

Figure 30. Comparison of viscoplastic deformation

All the test samples were subjected to the same load (60gf) for same amount of time (8 hours) under same environmental conditions (400^0C). The images shown in figure 30 clearly indicate that constitutive sample is much more resilient towards the time dependent mechanical deformation. While Subtractive UV sample showed very poor resistance against viscoplastic deformation, subtractive AC sample showed a much better resistance. This could be due to higher extent of crosslinking present in the Subtractive AC sample. As mentioned in chapter 2, Subtractive AC sample was cured in two stages. First the porogen was removed and then cross linking was initiated using the UV radiation. This means that this sample did not face any hindrance while cross linking reaction as all the porogen was already removed. However, in case of Subtractive UV sample cross linking and porogen removal was happening simultaneously which could have affected the extent of cross-linking in Subtractive UV sample. Lower cross linking would result in smaller clusters that can slide across each other under the influence of stress producing a viscous flow effect. [23]

Our previous studies also indicate that traditional subtractive films (equivalent to subtractive UV), with a much higher dielectric constant of 2.7 or much less porosity, exhibit high amount of viscoplastic deformation (see figure 10). [22], [23]

3.5 Molecular Structure

3.5.1 FTIR Analysis

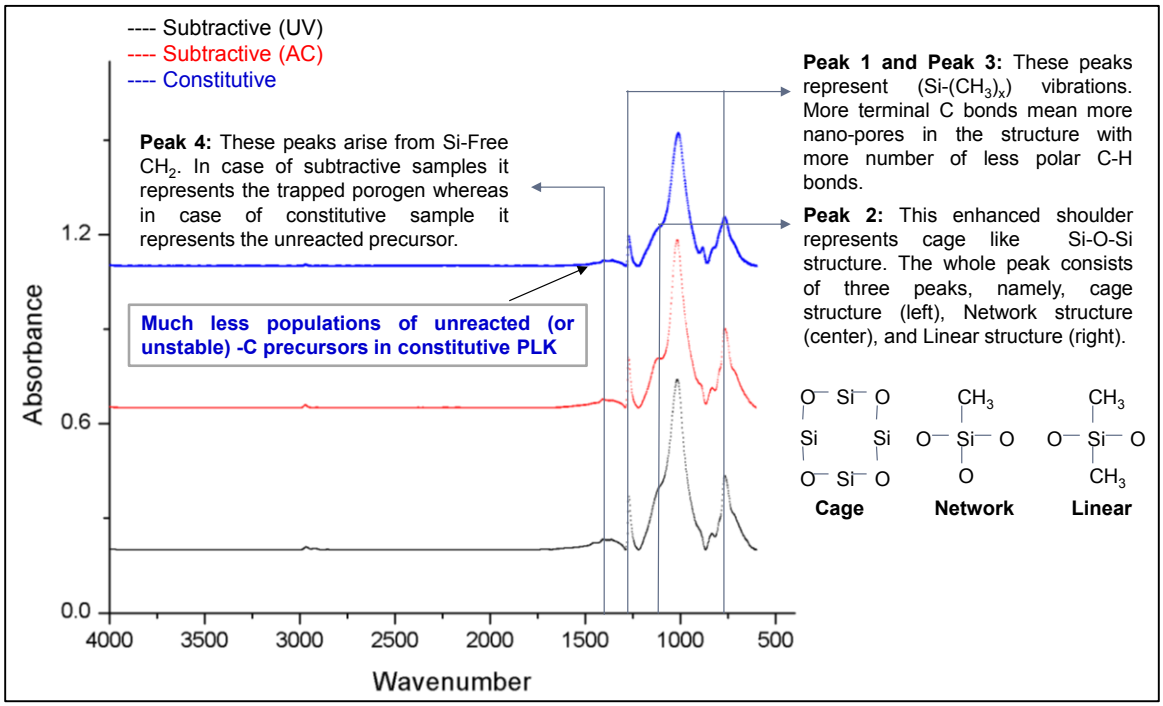

Figure 31. FTIR spectra of subtractive and constitutive films

To study the molecular structure of the samples, we collected the baseline corrected FTIR spectra for all the three samples. Si-O-Si peaks observed at ~1030 cm^{-1} are the most prominent peaks of these samples and represent the backbone structure of the films.[42] The very faint peak observed at ~2950 cm^{-1} represent CH_x (x = 1-3) vibrations.[42] These peaks are very faint because the relative amount of carbon in the structure is very low.

Peaks observed at 1380 cm^{-1} represent silicon free carbon or the carbon atoms that are not attached to the silicon atoms.[42] In the subtractive samples these peaks arise due to trapped labile porogen and in case of constitutive sample it represents unreacted carbon from the precursor. The peaks observed at 754 cm^{-1} and 1260 cm^{-1} represent Si-$(CH_3)_x$ vibrations.[42] Higher intensity ratio of these peaks to the Si-O-Si peaks means that the sample has high amount of terminal carbon bonds, which in turn means that the sample has more micro-pores in the matrix.

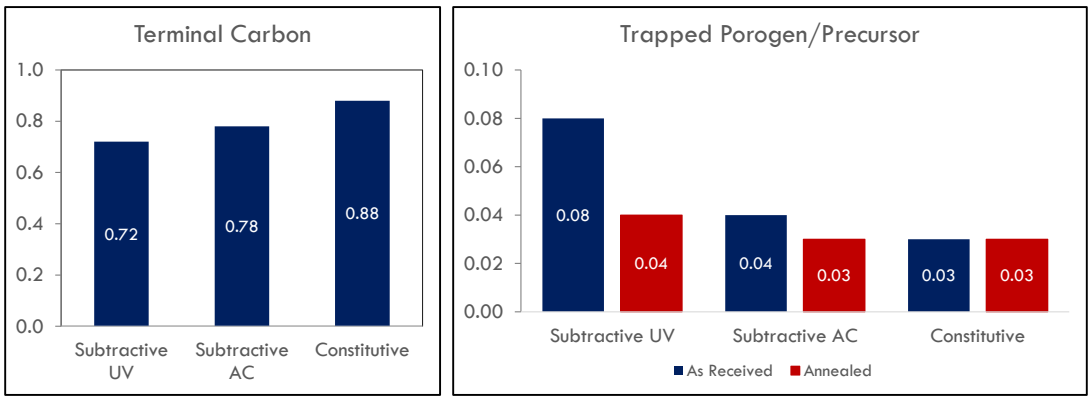

Figure 32. Comparison of (a) terminal carbon and (b) Si free carbon

We calculated the peak area ratio of various peaks, treating Si-O-Si peak as a reference peak, to compare the amount of terminal carbon and trapped porogen in our samples. The area ratio of (peak 1 + peak3) to peak 2 was calculated to compare the amount of terminal carbon. In order to compare the amount of trapped porogen/precursor, we measured the peak area ratio of peak 4 to peak 2. Figure 32 (a) shows the terminal carbon peak area ratio comparison. Based on the comparison we can say that the amount of terminal carbon in constitutive samples is more than the amount of the terminal carbon in subtractive sample. However this measure is not suitable to predict the exact quantity of

the terminal carbon, which is why this result is only used to compare the relative amounts across the sample.

Comparison of silicon free carbon peak area ratio in figure 32 (b) reveal that the amount of trapped porogen was highest in case of subtractive UV film and dielectric constant decrease observed after annealing process was because the trapped porogen was removed during annealing, which is evident from the decrease in the peak area ratio shown in figure 32 (b).

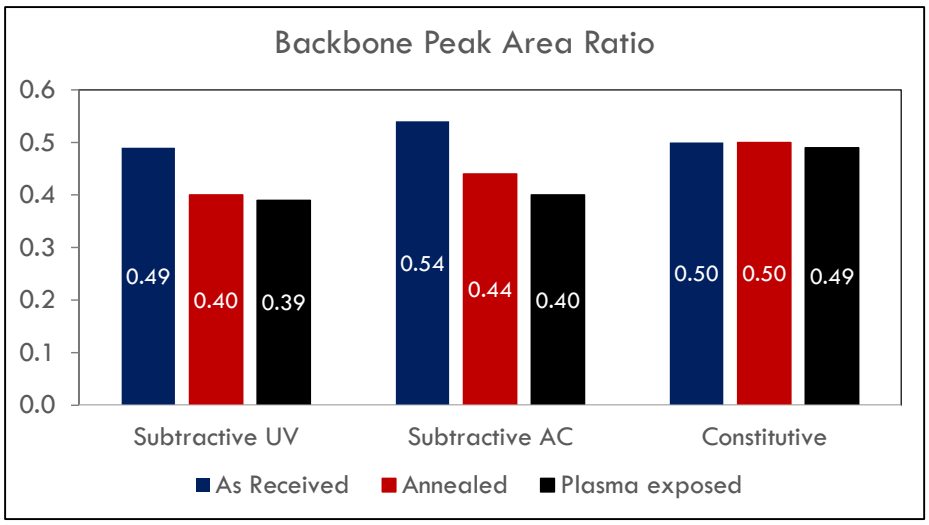

Figure 33. Peak area ratio of Si-O-Si bond

We also compared the effect of various treatments on the backbone structure of the dielectric material by comparing the change in peak area ratio of Si-O-Si peak to the cumulative area under the curve over the complete range of spectra for each sample. As illustrated in figure 33, constitutive sample doesn't show much change in the peak are ratio after annealing and plasma exposure. This shows that the constitutive sample is very stable during these treatments and the damage to the backbone is minimal. However, both the

subtractive samples suffered visible damage during these processes which is clearly evident from the graph.

Si-O-Si peak from the FTIR spectra is very useful for analyzing the backbone structure of the sample. This peak is a combination of three peaks

1. Cage structure peak
2. Network structure peak
3. Linear structure peak

Out of these three structures only the cage and linear structures are desirable. Cage structure is desired primarily due to its ability to provide more free volume with lesser damage to the mechanical properties as compared to the subtractive free volume. Cage structure has a very high Si-O-Si bond angle of about 150^0 and large cages are responsible for generating micro-pores in a structures along with terminal carbon bonds.[42] Although the cage structure is mechanically somewhat unstable as compared to the other two structures, it provides the material with the much desired free volume to bring down its dielectric constant. The deterioration in the mechanical properties in this case is far less than the alternative of subtractive free volume.

Linear structure is desirable primarily due to its ability to provide very high density and strong cross linking in the backbone structure while maintaining the symmetry. Symmetry helps in minimizing the dipole moment of the structure thus bringing down the dielectric constant of the material.[59] Although network structure can also provide very strong cross linking in the backbone, it lacks the symmetry and hence contributes towards the increase in dielectric constant of the overall material. Also, linear structure has more

terminal carbon bonds per silicon atom as compared to the network structure which means that it can provide more free volume within the structure along with better mechanical properties.

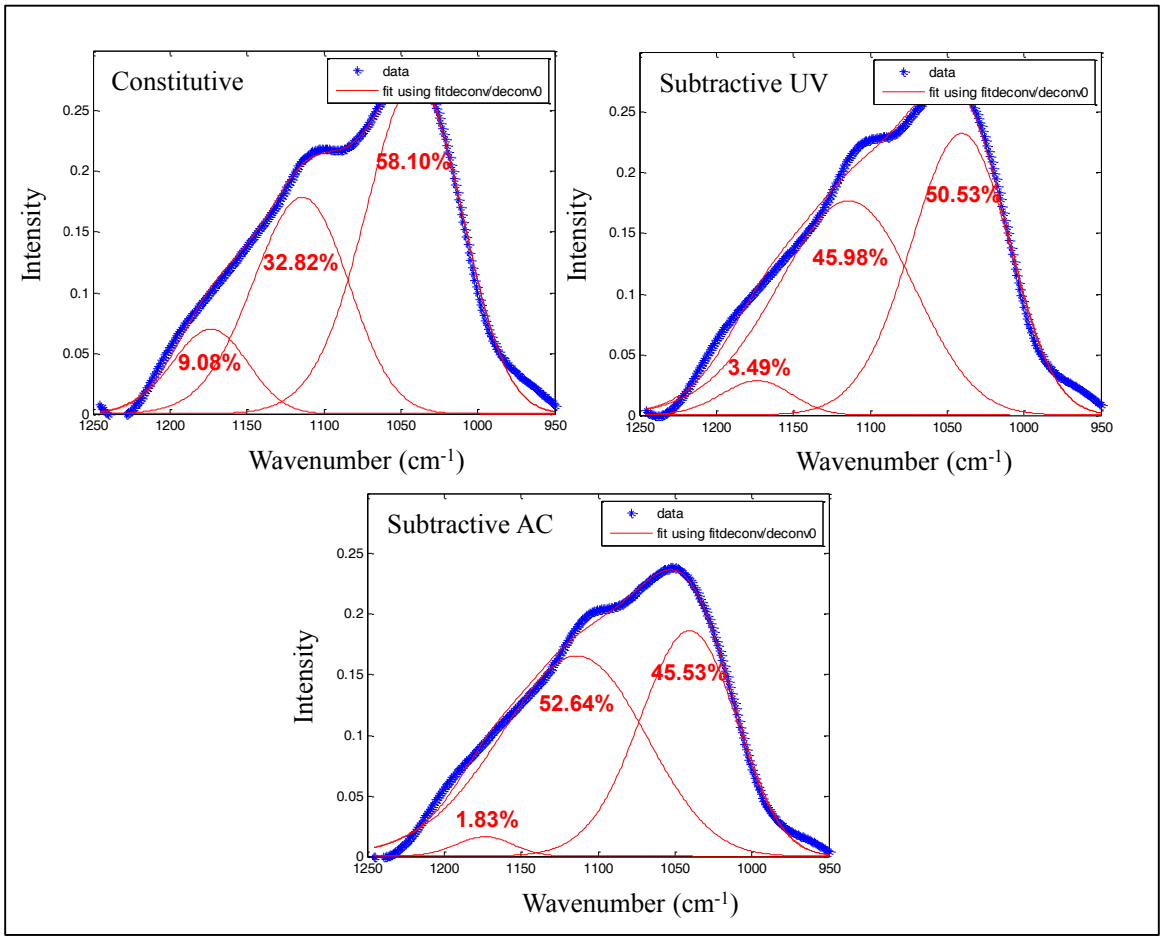

Figure 34. Deconvolution of Si-O-Si backbone peaks

Figure 34 shows the deconvoluted Si-O-Si peaks of the samples. It is clearly evident from the graphs that the constitutive sample is richer in the desired cage and linear structure whereas both the subtractive samples are richer in the undesired networked structure.

3.5.2 XPS Analysis

In order to gain more insight into the molecular structure of our samples, we collected the XPS spectra of both subtractive UV and Constitutive samples. Subtractive AC sample was not included in this study, however, we expect it to follow a trend similar to the Subtractive UV sample because structurally they both are very alike.

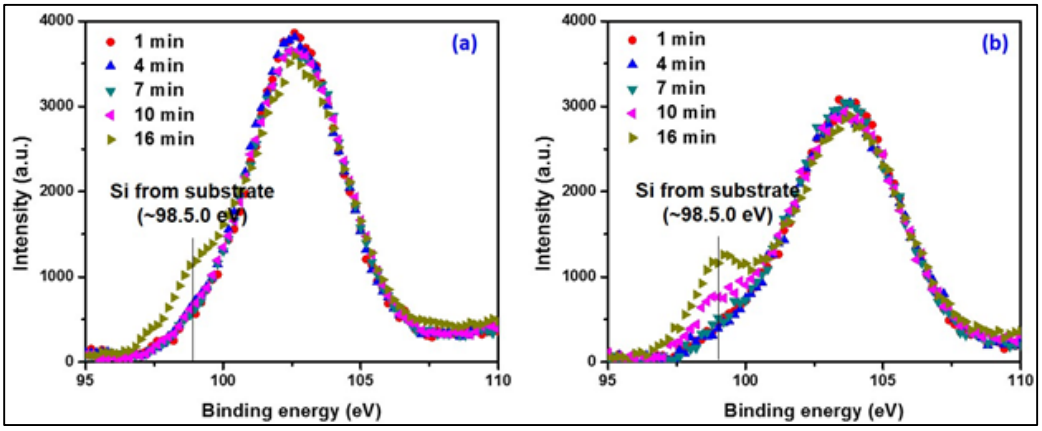

Figure 35. Depth profile of Si atom: (a) constitutive film, and (b) subtractive film

Figure 35 illustrates the depth profile of the silicon atoms in both the samples. Theoretically, the Si 2p spectra can be deconvoluted into 5 sub peaks:

- SiO_4 (104.9 eV)
- SiO_3 (103.7 eV)
- SiO_2 (102.6 eV)
- SiO_1 (101.7 eV), and
- SiO_0 (100.6 eV).[60]

The peak corresponding to 98.5 eV binding energy arises due to silicon present in the substrate. It is evident by the comparison of the two graphs that the silicon substrate

gets exposed first for subtractive film after about 10 min. of sputtering. In case of constitutive sample however, the peak was detected only after 16 min. of sputtering.

Another observation clearly evident from the comparison of the two graphs is that the intensity of peaks for constitutive samples is much higher than that of subtractive samples. This indicates higher amount of silicon bonds at the surface of the constitutive sample as compared to the subtractive samples. In other words, this simply indicates that the density of pores at the surface is much higher in case of subtractive sample as compared to the constitutive sample.

We also compared the shift in the peaks for the two samples by overlapping the Si 2p spectra of both of the films. As shown in figure 34 (a), the peaks for the two samples are quite apart from each other. Although the binding energy for the constitutive sample peak is lower than that of subtractive sample, higher intensity of the peak or higher density of the material in case of constitutive sample is the cause of its superior strength when compared to the subtractive sample.

The binding energy at which the peak occurs also gives important information about the specific backbone structure (cage, network, or linear) of the sample. The binding energy associated with the network structure, where silicon atom is connected to three oxygen atoms is higher than that associated with linear structure where silicon atom is connected only to two silicon atoms. This means that the subtractive film is rich in network structure whereas constitutive film has more network structure. This also means that constitutive film has more methyl per silicon as compared to the subtractive sample because network structure only has one methyl group per silicon atom whereas linear

structure has two methyl groups per silicon atom. Of course the assumption is that linear structure connected to methyl groups fully forming a chain like structure. [59]

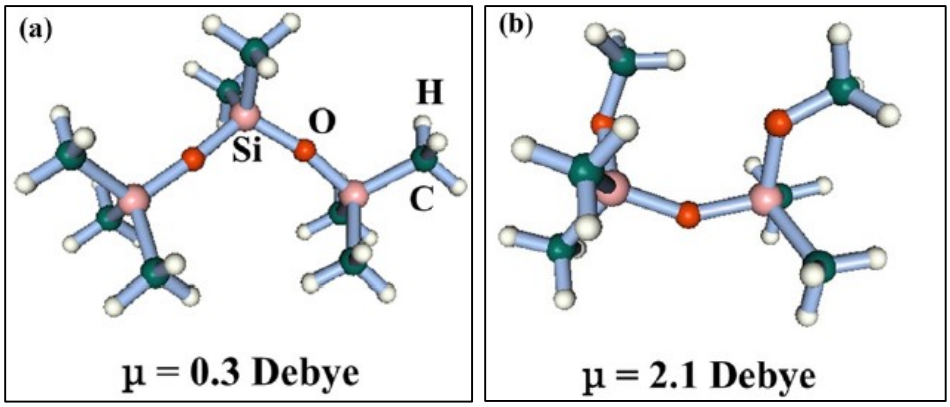

Figure 36. Dipole moment of (a) symmetric SiO_2 and (b) Asymmetric SiO_2 [59]

As illustrated in the figure 36, the symmetric bonding configuration in case of these chains reduces the dipole moment of the chain and more number of methyl groups bring more free volumes into the structure resulting in a low dielectric constant despite of the higher density of the overall material.

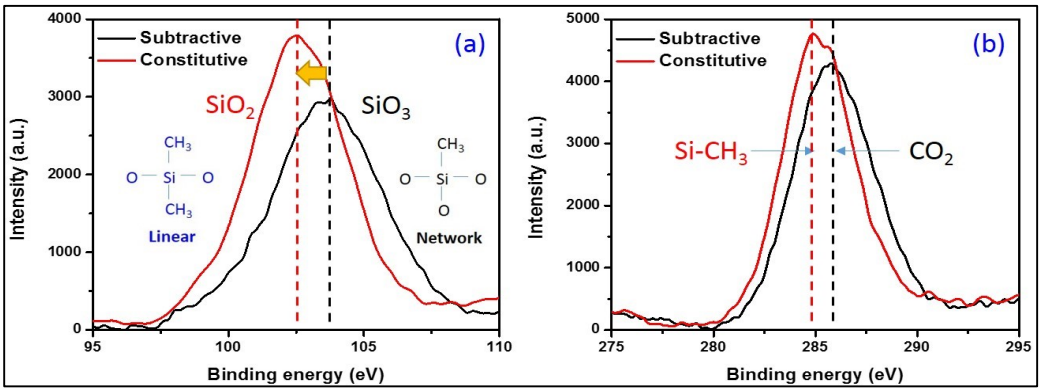

Figure 37. Comparison of XPS peak shift (a) Si 2p, and (b) C 1s

We also collected the C 1s spectra for both the samples which is shown in figure 37 (b). C 1s peak can be broken into four components:

- CSi_n (283.5 eV)
- $Si–CH_3$ (284.5 eV)
- CO_1 (285.3 eV), and
- CO_2 (286.3 eV).[60]

In case of constitutive film majority of the carbon was present in the form of methyl moieties whereas in case of subtractive film carbon was found to be attached to the oxygen. C-O bond is very polar and contributes towards increase of the overall dielectric constant of the material. Also, from the peak intensities, it is evident that constitutive film is richer in carbon content as compared to the subtractive film.

Chapter 4.

Conclusion

In order to keep up with the fast evolving technology, development of dielectric materials with lower dielectric constant is essential. However, dielectric constant is not the only property that one needs to look at. Other properties like mechanical strength and chemical stability are also equally vital for the material to be a viable replacement of current dielectric material. This thesis discussed the various properties of dielectric material that are important and how using alternative methods to reduce the dielectric constant of a material can result in a much better alternative for the replacement of traditional interlayer dielectric.

The samples were investigated for thickness and dielectric change after annealing and plasma damage. It was found that the constitutive sample showed much higher resistance to the damage caused by these two processes as compared to the subtractive samples primarily due to its closed and small pore structure. The closed and small pore structure kept the damage limited to the surface.

In terms of mechanical strength (hardness and modulus), constitutive sample was found to be the only option that can endure the stresses involved in the current industrial fabrication processes.

It has also been shown that a very small change in the curing method of traditional subtractive porous organosilicate dielectric film can result in a material that has significantly higher resistance to the viscoplastic deformation. Subtractive AC sample

showed excellent resistance towards viscoplastic deformation primarily due to better extent of crosslinking present in it as compared to the subtractive UV sample.

FTIR and XPS analyses of the samples revealed that constitutive samples are rich in desired cage and linear structures that reduce dielectric constant of the material through inherent reduction of dipole moment due to which the mechanical strength of the material is preserved. Table 6 summarizes the results of this thesis.

Table 6. Summary of results

	Subtractive UV	Subtractive AC	Constitutive
Porosity	Open pores	Open pores	Closed pores
	Non uniform	Non uniform	Slightly uniform
	Mesopores	Mesopores	Micropores
	Trapped porogen	No trapped porogen	
Thickness reduction	9% (Anneal)	8% (Anneal)	4% (Anneal)
	10% (Plasma)	10% (Plasma)	6% (Plasma)
Dielectric Change	(-5%) (Anneal)	1% (Anneal)	2% (Anneal)
	10% (Plasma)	10% (Plasma)	5% (Plasma)
Mechanical strength	6.2 GPa (E)	7.3 GPa (E)	13.4 GPa (E)
	1.3 GPa (H)	1.6 GPa (H)	2.2 GPa (H)
	Poor viscoplastic deformation resistance	Excellent viscoplastic deformation resistance due to strong crosslink	Negligible viscoplastic deformation

Table 6 — Continued

Bond structure	Less Terminal C	Rich in Network	More Terminal C
	Rich in Network	Rich in Linear	Rich in Cage
		Less Cage structure	Rich in Linear
Depth profile (subtractive UV vs. constitutive)	Low density Si network	High density Si network	
	Weaker film	Stronger film	

References

[1] R. H. Dennard, F. H. Gaensslen, H.-N. Yu, V. L. Rideovt, E. Bassous, and A. R. Leblanc, "Design of Ion-Implanted MOSFET with Very Small Physical Dimensions," *IEEE Solid-State Circuits Newsl.*, vol. 12, no. 1, 2007.

[2] D. Shamiryan, T. Abell, F. Iacopi, and K. Maex, "Low-k dielectric materials," *Mater. Today*, no. January, pp. 34–39, 2004.

[3] K. C. Saraswat and F. Mohammadi, "Effect of Scaling of Interconnections on the Time Delay of Vlsi Circuits.," *IEEE Trans. Electron Devices*, vol. 29, no. 4, pp. 645–650, 1982.

[4] K. Saraswat, "Interconnections : Copper & Low K Dielectrics," *Stanford Univ.*, no. EE311, 2003.

[5] T. Gupta, *Copper Interconnect Technology*. Springer New York, 2010.

[6] S. Beaudoin, S. Graham, R. Jaiswal, C. Kilroy, B. S. Kim, G. Kumar, and S. Smith, "An update on low-k dielectrics," *Interface*, vol. 14, no. 2, pp. 35–39, 2005.

[7] K. C. Aw and K. Ibrahim, "Characterisation of metal oxide semiconductor capacitor structure using low-k dielectric methylsilsesquioxane with evaporated aluminium and copper gate," *Thin Solid Films*, vol. 434, no. 1–2, pp. 178–182, 2003.

[8] H. Ruelke, P. Huebler, C. Streck, M. Gotuaco, and W. Senninger, "Implementation of CVD low-K dielectrics for high volume production," *Solid State Technol.*, p. 60, 2004.

[9] Y. Shioya, T. Ishimaru, H. Ikakura, Y. Nishimoto, T. Ohdaira, R. Suzuki, and K. Maeda, "Copper Barrier Properties of Low Dielectric Constant SiOCNH Film Deposited by Plasma-Enhanced CVD," *J. Electrochem. Soc.*, vol. 151, no. 1, p. C56, 2004.

[10] L. Trabzon and O. O. Awadelkarim, "C hanges in material properties of low- k interlayer dielectric polymers induced by exposure to plasmas," vol. 65, pp. 463–477, 2003.

[11] K. Maex, M. R. Baklanov, D. Shamiryan, F. Iacopi, S. H. Brongersma, and Z. S. Yanovitskaya, "Low dielectric constant materials for microelectronics," *J. Appl. Phys.*, vol. 93, no. 11, pp. 8793–8841, 2003.

[12] S. Lin, et al., *Proceedings of the Int. Interconnect Tech. Conf. (IITC 2001)*, p. 146-148.pdf.

[13] M. W. Lane, X. H. Liu, and T. M. Shaw, "Environmental effects on cracking and delamination of dielectric films," *IEEE Trans. Device Mater. Reliab.*, vol. 4, no. 2, pp. 142–147, 2004.

[14] E. G. Liniger and E. E. Simonyi, "Moisture-driven crack growth in blanket low dielectric constant and ultralow dielectric constant films," *J. Appl. Phys.*, vol. 96, no. 6, p. 3482, 2004.

[15] J. He, G. Xu, and Z. Suo, "Experimental determination of crack driving forces in integrated structures," *... 7th Int. Work. Stress. ...*, pp. 1–12, 2004.

[16] J. L. Beuth, "Cracking of thin bonded films in residual tension," *Int. J. Solids Struct.*, vol. 29, no. 13, pp. 1657–1675, 1992.

[17] G. Wang, C. Merrill, J. Zhao, S. K. Groothuis, and P. S. Ho, "Packaging Effects on Reliability of Cu / Low- k Interconnects," *IEEE Trans. Device Mater. Reliab.*, vol. 3, no. 4, pp. 119–128, 2003.

[18] F. Iacopi, S. . Brongersma, B. Vandevelde, M. O'Toole, D. Degryse, Y. Travaly, and K. Maex, "Challenges for structural stability of ultra-low-k-based interconnects," *Microelectron. Eng.*, vol. 75, no. 1, pp. 54–62, 2004.

[19] C. Waldfried, et al., *Proceedings of the Int. Interconnect Tech. Conf. (IITC 2002)*, p. 226-228.

[20] E. Mickler, et al., *Proceedings of the Int. Interconnect Tech. Conf. (IITC 2004)*, p. 190-192.

[21] H. Miyajima, et al., *Proceedings of the Int. Interconnect Tech. Conf. (IITC 2004)*, p. 222-224.

[22] Y. Sa, T. Ryan, S. King and C. Kim, "Restoration of Mechanical Stability and Dielectric Constants of Porous Low-k Dielectric by using Non-Oxidizing Plasma Treatment", *Semiconductor Research Corporation* , 2014.

[23] E. H. Zin, W. H. Bang, E. Todd Ryan, S. W. King, and C. U. Kim, "Study of viscoplastic deformation in porous organosilicate thin films for ultra low-k applications," *Appl. Phys. Lett.*, vol. 102, no. 22, pp. 2011–2015, 2013.

[24] A. Zenasni, V. Jousseaume, P. Holliger, L. Favennec, O. Gourhant, P. Maury, and G. Gerbaud, "The role of ultraviolet radiation during ultralow k films curing:

Strengthening mechanisms and sacrificial porogen removal," *J. Appl. Phys.*, vol. 102, no. 9, 2007.

[25] A. Delan, M. Rennau, S.E. Schulz and T. Gessner, *Microelectron. Eng.* 70 (2003) p. 280-284.

[26] T.-Y. Chiang, K. Banerjee and K.C. Saraswat, *Technical Digest. International Electron Devices Meeting, (IEDM 2000)*, p. 261-264.

[27] H. Miyajima, R. Katsumata, Y. Nakasaki, and Y. Nishiyama, "Water Absorption Properties of Fluorine-Doped SiO 2 Films Chemical Vapor Deposition Using Plasma-Enhanced," *Jpn. J. Appl. Phys.*, vol. 35, no. Part 1, No. 12A, pp. 6217–6225, 1996.

[28] S. J. Martin, J. P. Godschalx, M. E. Mills, E. O. Shaffer, and P. H. Townsend, "Development of a Low-Dielectric-Constant Polymer for the Fabrication of Integrated Circuit Interconnect," *Adv. Mater.*, vol. 12, no. 23, pp. 1769–1778, 2000.

[29] J. Yao, A. Iqbal, H. Juneja, and F. Shadman, "Moisture Uptake and Outgassing in Patterned and Capped Porous Low-k Dielectric Films," *J. Electrochem. Soc.*, vol. 154, no. 10, p. G199, 2007.

[30] A. Iqbal, H. Juneja, J. Yao, and F. Shadman, "Removal of moisture contamination from porous polymeric low-k dielectric films," *AIChE J.*, vol. 52, no. 4, pp. 1586–1593, 2006.

[31] Shaw, T.M., et al. *Advanced Metallization Conference 2003 Proceeding (AMC2003) 2003*. Montreal, Quebec, Canada and Tokyo, Japan Materials Research Society, Warrendale, PA.

[32] E. P. Guyer, J. Gantz, and R. H. Dauskardt, "Aqueous solution diffusion in hydrophobic nanoporous thin-film glasses," *J. Mater. Res.*, vol. 22, no. 03, pp. 710–718, 2007.

[33] T. Y. Tsui, A. J. McKerrow, and J. J. Vlassak, "The effect of water diffusion on the adhesion of organosilicate glass film stacks," *J. Mech. Phys. Solids*, vol. 54, no. 5, pp. 887–903, 2006.

[34] Y. Lin, T. Y. Tsui, and J. J. Vlassak, "Water diffusion and fracture in organosilicate glass film stacks," *Acta Mater.*, vol. 55, no. 7, pp. 2455–2464, 2007.

[35] A. a. Kumbhar, S. K. Singh, and R. O. Dusane, "Enhancement of moisture resistance of spin-on low-k HSQ films by hot wire generated atomic hydrogen treatment," *Thin Solid Films*, vol. 501, no. 1–2, pp. 329–331, 2006.

[36] H. Yanazawa, T. Fukuda, Y. Uchida, and I. Katou, "Water sorbability of low-k dielectrics measured by thermal desorption spectroscopy," *Surf. Sci.*, vol. 566–568, no. 1–3 PART 1, pp. 566–570, 2004.

[37] K. Yonekura, S. Sakamori, K. Goto, M. Matsuura, N. Fujiwara, and M. Yoneda, "Investigation of ash damage to ultralow-k inorganic materials," *J. Vac. Sci. Technol. B Microelectron. Nanom. Struct.*, vol. 22, no. 2, p. 548, 2004.

[38] D. Shamiryan, M. R. Baklanov, S. Vanhaelemeersch, and K. Maex, "Comparative study of SiOCH low-k films with varied porosity interacting with etching and cleaning plasma," *J. Vac. Sci. Technol. B Microelectron. Nanom. Struct.*, vol. 20, no. 5, p. 1923, 2002.

[39] E. Kondoh, T. Asano, a. Nakashima, and M. Komatu, "Effect of oxygen plasma exposure of porous spin-on-glass films," *J. Vac. Sci. Technol. B Microelectron. Nanom. Struct.*, vol. 18, no. 3, p. 1276, 2000.

[40] P. Ferrand, J. Seekamp, M. Egen, R. Zentel, S. G. Romanov, and C. M. S. Torres, "Direct electron-beam lithography on opal films for deterministic defect fabrication in three-dimensional photonic crystals," *Microelectron. Eng.*, vol. 73–74, pp. 362–366, 2004.

[41] Y. Furukawa, R. Wolters, H. Roosen, J. H. M. Snijders, and R. Hoofman, "Etch and strip induced material modification of porous low-k (k = 2.2) dielectric," *Microelectron. Eng.*, vol. 76, no. 1–4, pp. 25–31, 2004.

[42] A. Grill and D. a. Neumayer, "Structure of low dielectric constant to extreme low dielectric constant SiCOH films: Fourier transform infrared spectroscopy characterization," *J. Appl. Phys.*, vol. 94, no. 10, pp. 6697–6707, 2003.

[43] A. Dey and A. K. Mukhopadhyay, *Nanoindentation of Brittle Solids*. Taylor & Francis, 2014.

[44] X. Li and B. Bhushan, "A review of nanoindentation continuous stiffness measurement technique and its applications," *Mater. Charact.*, vol. 48, no. 1, pp. 11–36, 2002.

[45] A. Dey, P. Bandyopadhyay, and N. Biswas, "Nanoindentation: Why at All and Where?," pp. 39–44.

[46] Nair, R., Taylor, M., Binder, B., & Fischer, H. (2014). Measuring Hardness and More Through Nanoindentation. Retrieved June 2, 2015, from http://csmres.co.uk/cs.public.upd/article-downloads/Measuring-Hardness-and-More-through-Nanoindentation--Rahul-Nair-

[47] O'Neill, Hardness measurement of metals and alloys, London, Chapman and Hall, 1967.

[48] J. C. Hay, a. Bolshakov, and G. M. Pharr, "A critical examination of the fundamental relations used in the analysis of nanoindentation data," *J. Mater. Res.*, vol. 14, no. 06, pp. 2296–2305, 1999.

[49] I. N. Sneddon, "The relation between load and penetration in the axisymmetric boussinesq problem for a punch of arbitrary profile," *Int. J. Eng. Sci.*, vol. 3, no. 1, pp. 47–57, 1965.

[50] G. M. Pharr, "Measurement of mechanical properties by ultra-low load indentation," *Mater. Sci. Eng. A*, vol. 253, no. 1–2, pp. 151–159, 1998.

[51] R. M. a. Azzam, "Ellipsometry," *Handb. Opt. Third Ed. Vol. I Geom. Phys. Opt. Polariz. Light. Components Instruments*, pp. 1–26, 2009.

[52] R. S. Smith, *The effect of ultra-violet light curing on the molecular structure and fracture properties of an ultra low-k material*. ProQuest, 2007.

[53] Y. Lin, T. Y. Tsui, and J. J. Vlassak, "Octamethylcyclotetrasiloxane-Based, Low-Permittivity Organosilicate Coatings," *J. Electrochem. Soc.*, vol. 153, no. 7, p. F144, 2006.

[54] P. N. Sen and M. F. Thorpe, "Phonons in AX2 glasses: From molecular to band-like modes," *Phys. Rev. B*, vol. 15, no. 8, pp. 4030–4038, 1977.

[55] Günzler, H elmut, and Hans-Ulrich Gremlich. IR Spectroscopy: An Introduction . Weinheim: Wiley-VCH, 2002. Print.

[56] Horton, J. H. 'Chemical Force Spectrometry.' Dr. J. Hugh Horton » Research Projects . N.p., n.d. Web. 16 June 2015.

[57] Laurin, Mathias. 'Example: Principle of X-ray Photoelectron Spectroscopy (XPS).' Principle of X-ray Photoelectron Spectroscopy (XPS) . N.p., 26 Aug. 2009. Web. 16 June 2015.

[58] M. Miyoshi et al., *IITC Proc.*, 2003, p.57.

[59] Y. Kikuchi, A. Wada, T. Kurotori, M. Sakamoto, T. Nozawa, and S. Samukawa, "Non-porous ultra-low- k SiOCH (k = 2.3) for damage-free integration and Cu diffusion barrier," *J. Phys. D. Appl. Phys.*, vol. 46, no. 39, p. 395203, 2013.

[60] W. Wang, D. Grozea, A. Kim, D. D. Perovic, and G. A. Ozin, "Vacuum-Assisted Aerosol Deposition of a Low-Dielectric-Constant Periodic Mesoporous Organosilica Film," *Adv. Mater.*, vol. 22, no. 1, pp. 99–102, 2009.

Biographical Information

Akanksha Pandey was born in India. In 2012, she received her M.Sc. degree in chemistry from Indian Institute of technology, Bombay. She started pursuing her master's program in Materials Science and Engineering at the University of Texas at Arlington in 2013. During her stay at the University of Texas at Arlington, she worked as a research assistant in Prof. Choong-Un Kim's lab. Her research field was related to the characterization and comparison of mechanical properties of the porous low dielectric thin films.